

Monitoring the magnetospheric accretion of the classical T Tauri star DO Tau with SPIRou

J.-F. Donati¹, P.I. Cristofari², A. Carmona¹, A. Lavail¹, C. Moutou¹, J. Bouvier³, K. Perraut³, S.H.P. Alencar⁴, F. Ménard³, M. Audard⁵, P. Petit¹, E. Alecian³, T. Ray⁶, and the SPIRou science team

¹ Univ. de Toulouse, CNRS, IRAP, 14 avenue Belin, 31400 Toulouse, France (e-mail: jean-francois.donati@cnrs.fr)

² Leiden Observatory, Leiden University, Niels Bohrweg 2, 2333 CA Leiden, the Netherlands

³ Univ. Grenoble Alpes, CNRS, IPAG, 38000 Grenoble, France

⁴ Departamento de Física – ICEX – UFMG, Av. Antônio Carlos, 6627, 30270-901 Belo Horizonte, MG, Brazil

⁵ Department of Astronomy, University of Geneva, Chemin Pegasi, 51, Versoix CH-1290, Switzerland

⁶ Dublin Institute for Advanced Studies, Astronomy & Astrophysics Section, 31 Fitzwilliam Place, Dublin D02 XF86, Ireland

Submitted 2025 Dec. 19 – Accepted 2026 Feb. 22

ABSTRACT

We present observations of the classical T Tauri star DO Tau collected with the near-infrared SPIRou spectropolarimeter and precision velocimeter at the Canada-France-Hawaii Telescope from early 2020 to late 2025. Circularly polarized Zeeman signatures were clearly detected at most epochs in the atomic spectral lines of DO Tau, yielding longitudinal magnetic fields of up to 280 G modulated with a period of 5.128 ± 0.002 d which we identified as the rotation period of DO Tau. Applying Zeeman-Doppler imaging to the SPIRou data recorded in 2021, 2024 and 2025, we found that DO Tau hosts an unusual large-scale magnetic field that is weaker, less poloidal, more inclined to the rotation axis, and varies more rapidly with time than those of previously studied T Tauri stars, possibly as a result of intense accretion between the inner disk and the stellar surface. The dipole component of this large-scale field of about 0.2-0.3 kG even flipped polarity toward the end of our observing campaign, making DO Tau the first T Tauri star for which a magnetic polarity reversal is reported. The magnetospheric gap surrounding the central star was quite compact, extending to $\approx 1.6 R_*$ (0.014 au) as a result of the strong accretion rate ($\log \dot{M} = -7.7 M_{\odot} \text{ yr}^{-1}$), with the inner accretion disk being warped by the tilted stellar magnetic field. Radial velocity variations suggest the presence of a close-in planet of a few M_{J} or a density structure in the inner accretion disk at an orbital period of 21 d (corresponding to 0.12 au), which might be linked to the wiggle in the jet axis of DO Tau.

Key words. stars: magnetic fields – stars: formation – stars: low-mass – stars: individual: DO Tau – techniques: polarimetric

1. Introduction

With an age of only a few Myr, pre-main-sequence (PMS) low-mass T Tauri stars, and in particular the classical T Tauri stars (cTTs) that still accrete material from their accretion disk, are key targets for investigating the late phases of star formation and the multiple physical processes that take place in the close stellar environment, including magnetospheric accretion, outflows and jets (e.g., Romanova et al. 2021). They are also ideal objects for constraining models of planetary formation and migration at a stage for which very little observational material is yet available.

A few dozen weakly accreting cTTs have been observed at multiple epochs to address these points. We used spectropolarimetry to characterize the magnetic field of the central star and its interactions with the inner accretion disk, and velocimetry to investigate the potential presence of close-in massive companions at the outer edge of the stellar magnetospheres (e.g., Zaire et al. 2024; Donati et al. 2024d,b), in particular those transiting their host stars (Barber et al. 2024; Donati et al. 2025b). These results, some from data obtained with the near-infrared (nIR) SPIRou spectropolarimeter and velocimeter at the Canada-France-Hawaii Telescope (CFHT), used Zeeman-Doppler imaging (ZDI) to reconstruct the large-scale magnetic topologies of the observed cTTs. These data also clarify how magnetospheric accretion proceeds, emphasizing the role of magnetic fields in controlling the rotation of cTTs (Romanova et al. 2025).

Very few such studies exist for cTTs that strongly accrete material from their disks. Characterizing such an evolution phase, through which all PMS stars must go at some point (e.g., Fischer et al. 2023), is essential for a thorough understanding of star and planet formation. The effect of accretion flows on the formation of low-mass stars (e.g., Geroux et al. 2016), and more specifically, on the internal structure, convection patterns, dynamo processes, and large-scale magnetic fields, must be investigated to determine how these fields interact with accretion, outflows, and jets from the inner disks (Blinova et al. 2016), and how they affect stellar rotation (e.g., Amard & Matt 2023). In addition, detecting close-in massive planets and characterizing how they migrate within the disk and trigger enhanced accretion (Romanova et al. 2026) is essential for better constraining theoretical models at early stages of planet formation.

To address these points we ran a long-term observing program on DO Tau, a low-mass cTT with a high accretion rate, using SPIRou at the CFHT and collected spectra over 5.7 years. After recalling the main parameters of DO Tau and detailing the SPIRou observations we collected in Secs. 2 and 3, we model the temporal evolution of its magnetic field with Gaussian process regression (GPR) and ZDI in Secs. 4 and 5, and we investigate in Sec. 6 whether its radial velocity (RV) variations reveal the presence of a close-in massive planet. In Sec. 7 we study what the emission lines tell us about magnetospheric accretion taking place in DO Tau, and we summarize the results in Sec. 8.

2. The T Tauri star DO Tau

Located in the Taurus star-forming region (in the C7-L1527 spatial subgroup, aged 2.59 ± 0.75 Myr; Krolkowski et al. 2021) at a distance of 138.52 ± 0.68 pc from the Earth (Gaia Collaboration 2020), DO Tau is a low-mass M1 cTTS undergoing intense accretion as signaled by strong emission lines across its spectrum (Alcalá et al. 2021; Sousa et al. 2023). It is surrounded by a compact accretion disk of several dozen au that is inclined at $27.6 \pm 0.3^\circ$ to the line of sight (Long et al. 2019), whose inner region is the source of a CO outflow and a bipolar jet (e.g., Fernández-López et al. 2020; Erkal et al. 2021). Its complex circumstellar environment, featuring arms and streams, suggests an unusual evolution that might be caused by interactions with the nearby cTTS HV Tau or with remnant material from the star formation process (Winter et al. 2018; Huang et al. 2022). The morphology of the jet, and in particular the axis wiggle in both lobes, also suggests that the inner disk of DO Tau, from which the jet originates, might host a massive planet on an inclined orbit or be warped by a variable magnetic field (Erkal et al. 2021).

As DO Tau accretes material from the inner regions of its accretion disk at a relatively high rate, its spectrum is subject to veiling, i.e., a dilution of its photospheric lines that results from the addition of a mostly featureless spectral contribution from warm accretion features (strongest in the blue) and from the inner edge of the accretion disk (strongest in the red). Photospheric spectral lines of DO Tau can thus be weaker by two to seven times than expected from a weak-line TTS of the same spectral type (Alcalá et al. 2021, see also Sec. 7), rendering fundamental parameters hard to estimate precisely. Several studies quoted values inferred from high-resolution spectra, e.g., Alcalá et al. (2021) who derived an effective temperature of $T_{\text{eff}} = 3694 \pm 104$ K from optical spectra and López-Valdivia et al. (2021) who reached similar results with larger error bars from nIR spectra ($T_{\text{eff}} = 3704 \pm 350$ K and $\log g = 3.44 \pm 0.50$ dex). A study from low-resolution spectra aimed at explaining the *IYJ* continuum excess emission of cTTSs suggested a much lower effective temperature ($T_{\text{eff}} = 2947 \pm 25$ K; Pérez Paolino et al. 2025). Our own analysis of the least veiled SPIRou spectra yielded an intermediate value ($T_{\text{eff}} = 3450 \pm 50$ K and $\log g = 3.6 \pm 0.1$ dex, see Sec. 3), which is more or less consistent with previous measurements from high-resolution spectroscopy.

The velocity field in the disk derived from molecular line ALMA images indicated a dynamical mass of $M_\star = 0.54 \pm 0.07 M_\odot$ for DO Tau (Braun et al. 2021), which, when it is coupled to our estimate of $\log g$ implied a stellar radius of $R_\star = 1.9 \pm 0.2 R_\odot$ and a logarithmic luminosity of $\log L_\star/L_\odot = -0.3 \pm 0.2$. The original evolutionary models of Feiden (2016) that include magnetic fields are able to reconcile our T_{eff} and $\log g$ estimates with this mass measurement, yielding an age of 1.7 ± 0.5 Myr (consistent with that of the C7-L1527 Taurus subgroup). In their most recent version (where the surface magnetic field strength was updated at each model iteration to be equal to the pressure equipartition value; Feiden, private communication), the mass that best matches our measurements is $0.42 \pm 0.05 M_\odot$, slightly lower than (but still compatible with) the dynamical mass estimate of DO Tau. The nonmagnetic models of Feiden (2016) and those of Baraffe et al. (2015) yield an even lower mass of 0.30 – $0.32 M_\odot$, which is inconsistent with the dynamical estimate. DO Tau is still fully convective according to evolutionary models of Feiden (2016), although convection might be affected by strong accretion (Geroux et al. 2016).

Our spectropolarimetric observations of DO Tau with SPIRou (see Secs. 3 and 4) revealed that the stellar rotation pe-

Table 1: Parameters of DO Tau

distance (pc)	138.52 ± 0.68	Gaia Collaboration (2020)
T_{eff} (K)	3450 ± 50	this paper
$\log g$ (cm s $^{-2}$)	3.60 ± 0.10	this paper
M_\star (M_\odot)	0.54 ± 0.07	Braun et al. (2021)
R_\star (R_\odot)	1.9 ± 0.2	this paper
$\log L_\star/L_\odot$	-0.3 ± 0.2	this paper
age (Myr)	1.7 ± 0.5	Feiden (2016)
P_{rot} (d)	5.128 ± 0.002	this paper
$v \sin i$ (km s $^{-1}$)	13.0 ± 0.5	this paper
i ($^\circ$)	45 ± 8	from P_{rot} , $v \sin i$, and R_\star
i_{disk} ($^\circ$)	27.6 ± 0.3	Long et al. (2019)
$\langle B \rangle$ (kG)	2.5 ± 0.3	this paper
r_{cor} (R_\star , au)	5.4, 0.047	from P_{rot} , M_\star , and R_\star
$\log \dot{M}$ (M_\odot yr $^{-1}$)	-7.70 ± 0.19	this paper
RV (km s $^{-1}$)	16.3 ± 0.1	this paper

riod is $P_{\text{rot}} = 5.128 \pm 0.002$ d and the rotational broadening of spectral lines is $v \sin i = 13.0 \pm 0.5$ km s $^{-1}$, implying an inclination angle i of the stellar rotation axis to the line of sight of $i = 45 \pm 8^\circ$, consistent with the inclination of the inner disk from interferometric measurements (Perraut et al. 2025). This is higher than the inclination of the outer disk and is an additional indication that the evolution history of DO Tau is complex and that its inner disk is warped. Table 1 lists the parameters we used.

DO Tau is known to exhibit significant Zeeman broadening of photospheric lines, which is attributed to small-scale magnetic fields at the surface of the star with an average strength $\langle B \rangle = 1.78 \pm 0.85$ kG (López-Valdivia et al. 2021). Zeeman signatures were also detected in the 588 nm He I line of DO Tau, demonstrating a magnetic field of 0.45 – 0.79 kG at the footpoints of the magnetospheric accretion funnels linking the star to the inner disk (Dodin et al. 2013).

Several studies estimated mass accretion at the surface of DO Tau, in most cases by exploiting accretion fluxes derived from several emission lines using calibrated scaling laws (Alcalá et al. 2017; Fiorellino et al. 2025). Measuring accretion fluxes in 16 emission lines from the UV to the nIR, Alcalá et al. (2021) obtained that $\log \dot{M} = -7.73 \pm 0.40$ (with \dot{M} in M_\odot yr $^{-1}$). From SPIRou spectra (some in common with our study), Sousa et al. (2023) obtained a similar estimate ($\log \dot{M} = -7.54 \pm 0.30$) using Pa β and Bry alone. Along with the strong veiling, it demonstrates that DO Tau is one of the strongest cTTS accretors in its mass range (see Fig. 9 of Alcalá et al. 2021).

DO Tau was monitored by TESS in 2021 (September 6 to November 6, sectors 43 and 44) and 2023 (September 20 to November 11, sectors 70 and 71) and exhibited a chaotic and aperiodic light curve of amplitude ≈ 1 mag, consistent with the K2 light curve based on which DO Tau was classified as a burster with photometric variations mostly attributed to accretion processes and not to rotational modulation (Cody et al. 2022).

3. SPIRou observations

We observed DO Tau between 2020 February 19 and 2025 November 13, with the SPIRou nIR spectropolarimeter (Donati et al. 2020) at the CFHT, within the SPIRou Legacy Survey and the SPICE and PLANETS large programs (RUNIDs 20AP40, 20BP40, 23AP45, 23BP45, 24AP45, and 25BP45, PI J.-F. Donati). SPIRou collects unpolarized and polarized stellar spectra, covering a range of 0.95 – $2.50 \mu\text{m}$ at a resolving power of 70 000 in a single exposure. Polarimetric observations con-

sist of a sequence of four subexposures, with each subexposure corresponding to a different azimuth of the Fresnel rhomb retarders of the SPIRou polarimetric unit. With this procedure, we are able to remove systematics in polarized spectra to first order (Donati et al. 1997). For DO Tau, we focused on circular polarization, each recorded sequence of four subexposures yielding one unpolarized (Stokes I) and one circularly polarized (Stokes V) spectrum, as well as one null polarization check (called N) used to diagnose potential instrumental or data reduction issues. We collected 77 polarization sequences over five consecutive observing seasons covering 2094 d, 3 in early 2020, 8 in late 2020 – early 2021, 3 in early 2023, 20 in early 2024, and 43 in late 2025. The total exposure times ranged from 1582 to 1627 s, while the signal-to-noise ratios (S/Ns) per 2.3 km s^{-1} pixel in the H band ranged from 154 to 321 (median 260).

All spectra were processed with *Libre ESPrIT*, the nominal reduction pipeline of ESPaDOnS at CFHT, optimized for spectropolarimetry and adapted for SPIRou (Donati et al. 2020). To all reduced spectra, we applied least-squares deconvolution (LSD; Donati et al. 1997) using a line mask computed with the VALD-3 database (Ryabchikova et al. 2015) for atmospheric parameters matching those of DO Tau ($T_{\text{eff}} = 3500 \text{ K}$, $\log g = 3.5$). We only selected atomic lines deeper than 10% of the continuum level I_c (with negligible contribution from the disk) for a total of ≈ 1500 lines with an average wavelength and Landé factor equal to 1750 nm and 1.2 . This yielded noise levels, σ_V , in the resulting Stokes V LSD profiles ranging from 1.6 to 4.1 (median 2.1), in units of $10^{-4}I_c$. Zeeman signatures were detected at most epochs, with typical peak-to-peak amplitudes of a few 0.1%. We computed the longitudinal field B_ℓ (i.e., the line-of-sight component of the magnetic vector averaged over the visible stellar hemisphere, an ideal proxy for diagnosing rotational modulation; e.g., Rescigno et al. 2024) from LSD Stokes I and V profiles following Donati et al. (1997), integrating over an interval of $\pm 30 \text{ km s}^{-1}$ adequate for DO Tau. We found that B_ℓ was well detected, and the reduced chi square assuming no field was $\chi_r^2 = 43$. The same operation applied to the null polarization spectrum N yielded $\chi_r^2 = 0.81$, which is consistent with no spurious signal and indicates no issues in the observation and reduction procedures. B_ℓ ranged from -193 to 276 G (median error bar 19 G , see Fig. 1 and Sec. 4) and was clearly rotationally modulated. We also computed Stokes I LSD profiles with a line mask that only included the magnetically insensitive CO bandhead lines from 2.29 to $2.40 \mu\text{m}$ deeper than 10% of I_c (≈ 500 lines), seen in absorption and coming mostly from the star, to examine how they differed from the LSD profiles of atomic lines.

We also reduced our SPIRou data with the latest version of APERO (v0.7.294), the nominal SPIRou reduction pipeline (Cook et al. 2022) optimized for RV precision and the correction of telluric lines. We applied the line-by-line (LBL) technique (v0.65; Artigau et al. 2022) to the reduced data, yielding RVs and differential temperatures dT estimated from variations in the relative depths of veiling-corrected spectral lines with respect to their median profiles (Artigau et al. 2024). However, LBL was designed for measuring subtle changes in stellar spectra and might not be well suited for highly veiled cTTs like DO Tau. We found that while LBL RVs show a clear rotational modulation (see Sec. 6), dT is only marginally modulated at P_{rot} with a periodogram peaking at 12.9 d and showing several peaks of similar strength between 5 and 30 d . We also applied LSD to the APERO spectra with the masks mentioned above and derived alternative RVs, separately for atomic and CO bandhead lines, by describing each individual LSD profile as a simple first-order Taylor expansion constructed from the median of all LSD

profiles (as in previous studies; e.g., Donati et al. 2024b,a). The LBL RVs were found to correlate tightly with the RVs of CO lines (Pearson’s coefficient $R \approx 0.90$) and more loosely with those of atomic lines ($R \approx 0.80$), but showed a significantly weaker modulation amplitude than either (see Sec. 6).

We used the median of the least veiled APERO-reduced spectra of DO Tau to measure the stellar parameters with ZeeTurbo (Cristofari et al. 2023) simultaneously with the small-scale magnetic field estimated from the Zeeman broadening of the spectral lines. For the stellar parameters, we found $T_{\text{eff}} = 3450 \pm 50 \text{ K}$ and $\log g = 3.60 \pm 0.10$ (assuming solar metallicity). We also deduced that DO Tau hosts a small-scale magnetic field of $\langle B \rangle = 2.5 \pm 0.3 \text{ kG}$, with the 2 and 4 kG components covering 85% and 8% of the visible hemisphere on average, and the other (including the field-free component) contributing less than a few percent. This is stronger than the value derived by López-Valdivia et al. (2021, equal to $1.78 \pm 0.85 \text{ kG}$), possibly due to long-term evolution. Given the strong veiling, individual spectra were too noisy for ZeeTurbo to yield reliable results.

The full log of our observations is provided in Table A.1. Phases and rotation cycles were derived assuming a rotation period of $P_{\text{rot}} = 5.128 \text{ d}$ (see Table 1), counting from an arbitrary starting barycentric Julian date (BJD) of $2\,458\,898.7$ (slightly before our first observation of DO Tau).

4. Magnetic field and temperature changes

To quantify the temporal fluctuations of B_ℓ , arranged in a vector denoted y , we applied GPR (Haywood et al. 2014; Rajpaul et al. 2015) and employed the following quasi-periodic (QP) covariance function $c(t, t')$

$$c(t, t') = \theta_1^2 \exp \left(-\frac{(t - t')^2}{2\theta_3^2} - \frac{\sin^2 \left(\frac{\pi(t - t')}{\theta_2} \right)}{2\theta_4^2} \right) \quad (1)$$

where θ_1 is the amplitude (in G) of the Gaussian process (GP), θ_2 is its recurrence period (measuring P_{rot}), θ_3 is the evolution timescale on which the B_ℓ curve changes shape (in d), and θ_4 is a smoothing parameter controlling the amount of harmonic complexity. A fifth hyperparameter, θ_5 , describes the excess of uncorrelated noise on B_ℓ . This ensures that the QP GPR fit can diagnose cases where the standard error bars are underestimated, and reach the solution with highest likelihood, \mathcal{L} , defined by

$$2 \log \mathcal{L} = -n \log(2\pi) - \log |C + \Sigma + S| - y^T (C + \Sigma + S)^{-1} y \quad (2)$$

where C is the covariance matrix for all observing epochs, Σ is the diagonal variance matrix associated with y , $S = \theta_5^2 J$ is the contribution of the additional white noise, with J the identity matrix, and n is the number of data points.

We explored the hyperparameter domain with a Markov chain Monte Carlo (MCMC) process and retrieved posterior distributions and error bars for all parameters. The MCMC and GPR modeling tools were those used in our previous studies (e.g., Donati et al. 2023). The MCMC process is a single-chain Metropolis-Hastings scheme running over a few 10^5 steps, including the first few 10^4 steps as burn-in. Convergence was checked with an autocorrelation analysis to verify that the burn-in and main phase vastly exceeded the autocorrelation lengths of all parameters. We computed the marginal logarithmic likelihood, $\log \mathcal{L}_M$, following Chib & Jeliazkov (2001).

The GPR fit we obtained is shown in Fig. 1, with a zoom-in on the 2025 data. The derived GPR hyperparameters are listed in Table 2. The rotation period we infer ($5.128 \pm 0.002 \text{ d}$) is

Table 2: MCMC GPR modeling of the B_ℓ curve of DO Tau

Parameter	Symbol	Value	Prior
GP amplitude (G)	θ_1	159 ± 48	mod Jeffreys (σ_{B_ℓ})
Rec. period (d)	θ_2	5.128 ± 0.002	Gaussian (5.1, 1.0)
Evol. timescale (d)	θ_3	600	fixed
Smoothing	θ_4	0.87 ± 0.21	Uniform (0, 3)
White noise (G)	θ_5	22.6 ± 3.6	mod Jeffreys (σ_{B_ℓ})
Rms (G)		25.4	
χ_r^2		1.83	

Notes. For each hyper parameter, we list the fitted value along with the corresponding error bar and the assumed prior. The knee of the modified Jeffreys prior is set to the median error bar of B_ℓ (19 G). The evolution timescale θ_3 was poorly constrained by the data and set to 600 d.

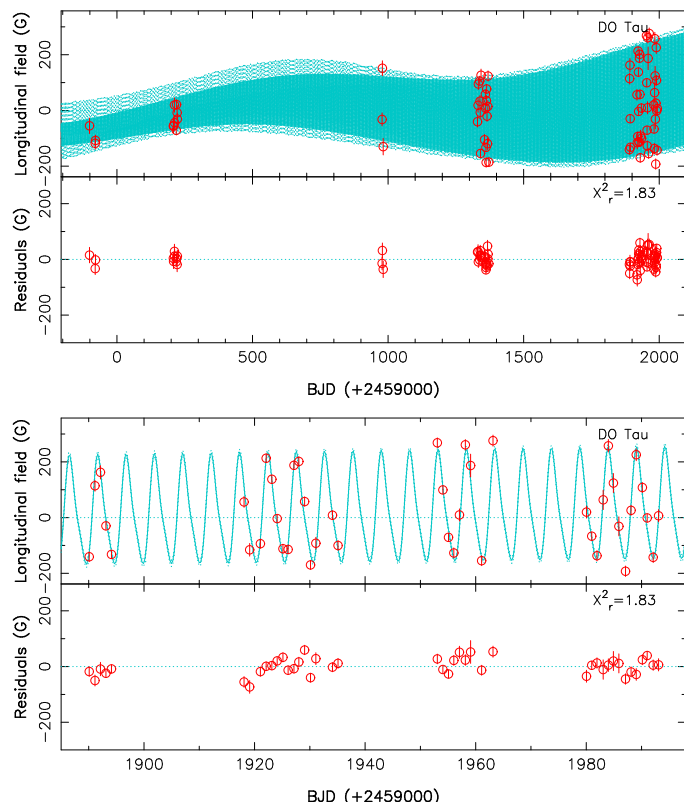


Fig. 1: Longitudinal magnetic field B_ℓ (red dots), and QP GPR fit to the data (full cyan line) with corresponding 68% confidence intervals (dotted cyan lines). The bottom panel zooms in on the 2025 data. The residuals, shown in the bottom plot of each panel, have an rms of 25 G ($\chi_r^2 = 1.8$).

shorter than that of prototypical mildly accreting cTTs (e.g., AA Tau or BP Tau) and agrees better with that of lower-mass cTTs (e.g., V2247 Tau, Donati et al. 2010) and strong accretors (e.g., RU Lup, Armeni et al. 2024). The rotational modulation semi-amplitude of B_ℓ increased steadily, growing from ≈ 50 G in 2020 to ≈ 200 G in 2025. B_ℓ progressively evolved from being always or mostly negative in 2020 (average -94 G) and 2021 (average -28 G) to mostly positive in 2025 (average 24 G). Given the good sampling in three of our five seasons, this suggests a topological change in the large-scale field of DO Tau over our observing campaign. The poloidal field component (to which B_ℓ is mostly sensitive) was slightly tilted to the stellar rotation axis in 2020 (given the low-amplitude modulation with respect to the average $|B_\ell|$; see Fig. 1), became more tilted in 2021 and 2024

(lower average $|B_\ell|$ and stronger modulation), and was even more strongly tilted in 2025 following a polarity switch (maximum amplitude modulation and sign change of the average B_ℓ ; see Fig. 1). The achieved χ_r^2 (1.83) is significantly larger than 1, indicating that intrinsic variability, likely due to accretion, induced random variations in B_ℓ stronger than those from photon noise.

We carried out a similar analysis on dT and confirmed that rotational modulation was marginal. The semi-amplitude of dT fluctuations was only ≈ 7 K (rms 14 K) and roughly constant with time, indicating that surface brightness features (brighter or darker than the photosphere) were either too small or the contrast was too low to induce detectable rotational modulation.

5. ZDI modeling

We applied ZDI to the LSD Stokes I and V profiles of DO Tau to model the rotational modulation of the line profiles, assuming their shapes and distortions are caused by brightness and magnetic surface features. As in previous studies, LSD profiles were corrected for veiling to remove contributions from accretion funnels, flares and the inner disk to first order. For highly veiled cTTs, however, occultation by dense accretion funnels or strong warps in the inner accretion disk (e.g., induced by highly tilted magnetic fields, Romanova et al. 2003) might also generate profile distortions resembling those induced by brightness features; we did not include this option in the modeling to avoid making it overly complex by adding still more free parameters, but we kept it in mind when we analyzed the ZDI results. Of the five seasons for which we collected data, only two (2024 and 2025) featured a dense phase coverage to allow reliable brightness and magnetic imaging with ZDI, with a third season (2021) for which sparser sampling was achieved but on which we still applied ZDI (we kept in mind this caveat when discussing the results). Using both LSD Stokes I and V (instead of only Stokes V) profiles in the ZDI modeling ensures that the Zeeman broadening of line profiles is taken into account and that the reconstructed field is not severely underestimated (e.g., Donati et al. 2025a).

In practice, ZDI operates as outlined in previous studies. Beginning with empty magnetic maps and brightness distributions and assuming that the star rotates as a solid body, ZDI iteratively adds information on both images, exploring the parameter space with conjugate gradient techniques and comparing the synthetic Stokes profiles of the current images with observed ones at each iteration, until it reaches the requested level of agreement with the data (i.e., a given χ_r^2). The surface of DO Tau was divided into 5000 grid cells, each associated with a value of the local surface brightness (relative to the quiet photosphere). We proceeded in a different way for the magnetic field, described as a spherical harmonics (SH) expansion using the formalism of Donati et al. (2006) in its revised implementation (Lehmann & Donati 2022; Finociety & Donati 2022), where the poloidal and toroidal components of the vector field are expressed with three sets of complex SH coefficients, $\alpha_{\ell,m}$ and $\beta_{\ell,m}$ for the poloidal component, and $\gamma_{\ell,m}$ for the toroidal component (ℓ and m denoting the degree and order of the corresponding SH term in the expansion). We limited the SH expansion to $\ell = 10$, consistent with the measured $v \sin i$ (see Table 2). The inversion problem is ill-posed and requires some regularization as the number of parameters is much larger than the number of independent data points. ZDI chooses the simplest solution, i.e., the solution with minimum information or maximum entropy that matches the data at the requested χ_r^2 level, following Skilling & Bryan (1984).

Local synthetic Stokes I and V profiles for each grid cell were computed using Unno-Rachkovsky's solution of the po-

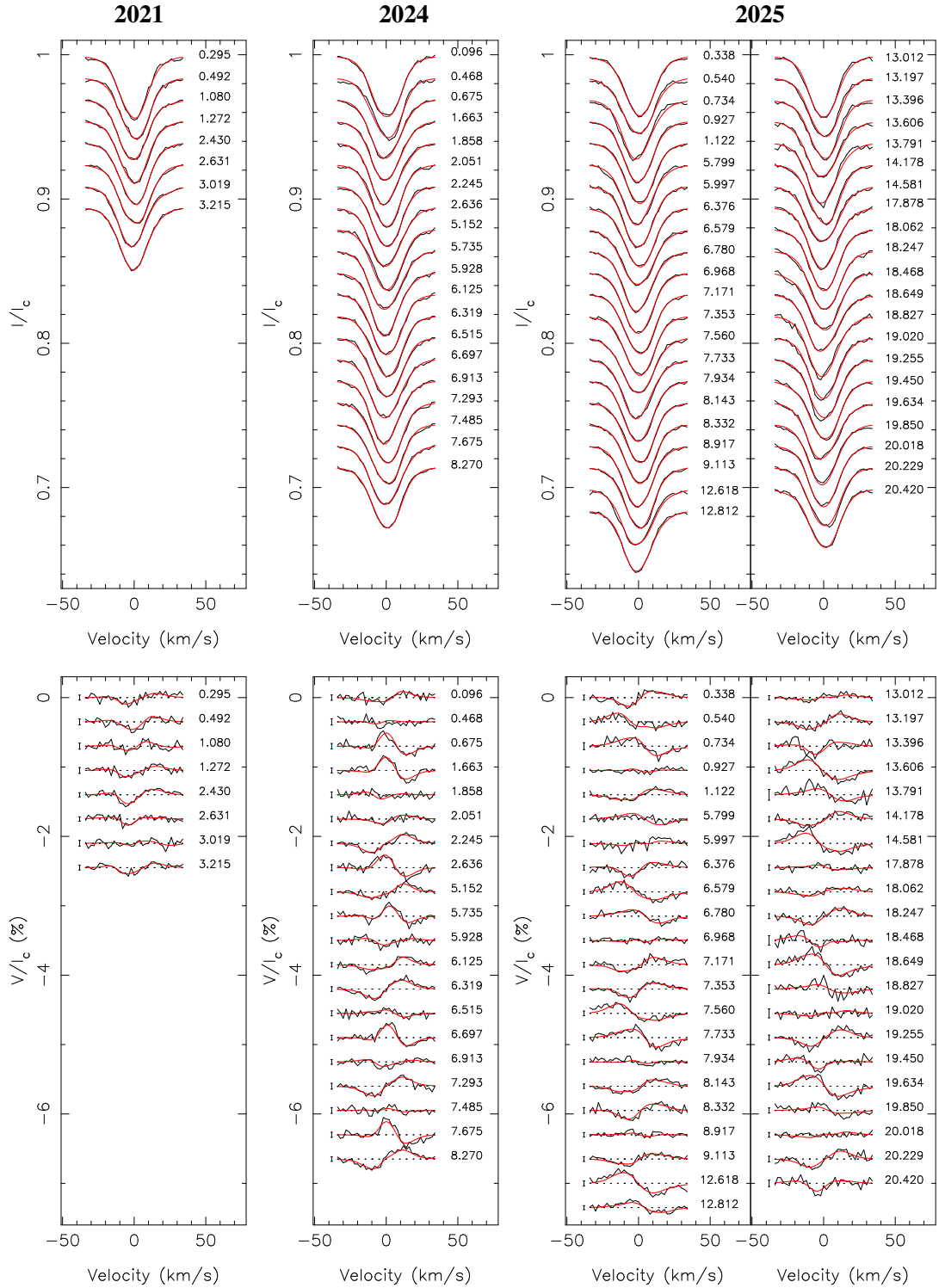


Fig. 2: Observed (thick black line) and modeled (thin red line) LSD Stokes I (top row) and V (bottom row) profiles of DO Tau in 2021, 2024, and 2025 (from left to right). Rotation cycles (counting from 60, 279, and 388 in 2021, 2024, and 2025, respectively, see Table A.1) are indicated to the right of the LSD profiles, and $\pm 1\sigma$ error bars are shown to the left of the Stokes V profiles.

larized radiative transfer equation in a plane-parallel Milne-Eddington atmosphere (Landi degl'Innocenti & Landolfi 2004), and assuming a linear center-to-limb darkening law for the continuum (with a coefficient of 0.3). At each observed rotation phase, the spectral contributions from all visible cells were summed to obtain the overall synthetic profiles, whose mean wavelength and Landé factor mirror those of our LSD profiles

(1750 nm and 1.2). We assumed a Doppler width of the local profile of $v_D = 3.0 \text{ km s}^{-1}$, typical for such stars. As in previous studies, we introduced a filling factor for the large-scale field, f_V , and another for the small-scale field, f_l , both assumed constant over the star. This implies that each cell with a reconstructed field B hosts a field strength B/f_V in a fraction of the cell equal to f_V (f_l) for Stokes V (I) LSD profiles. For this study, we set

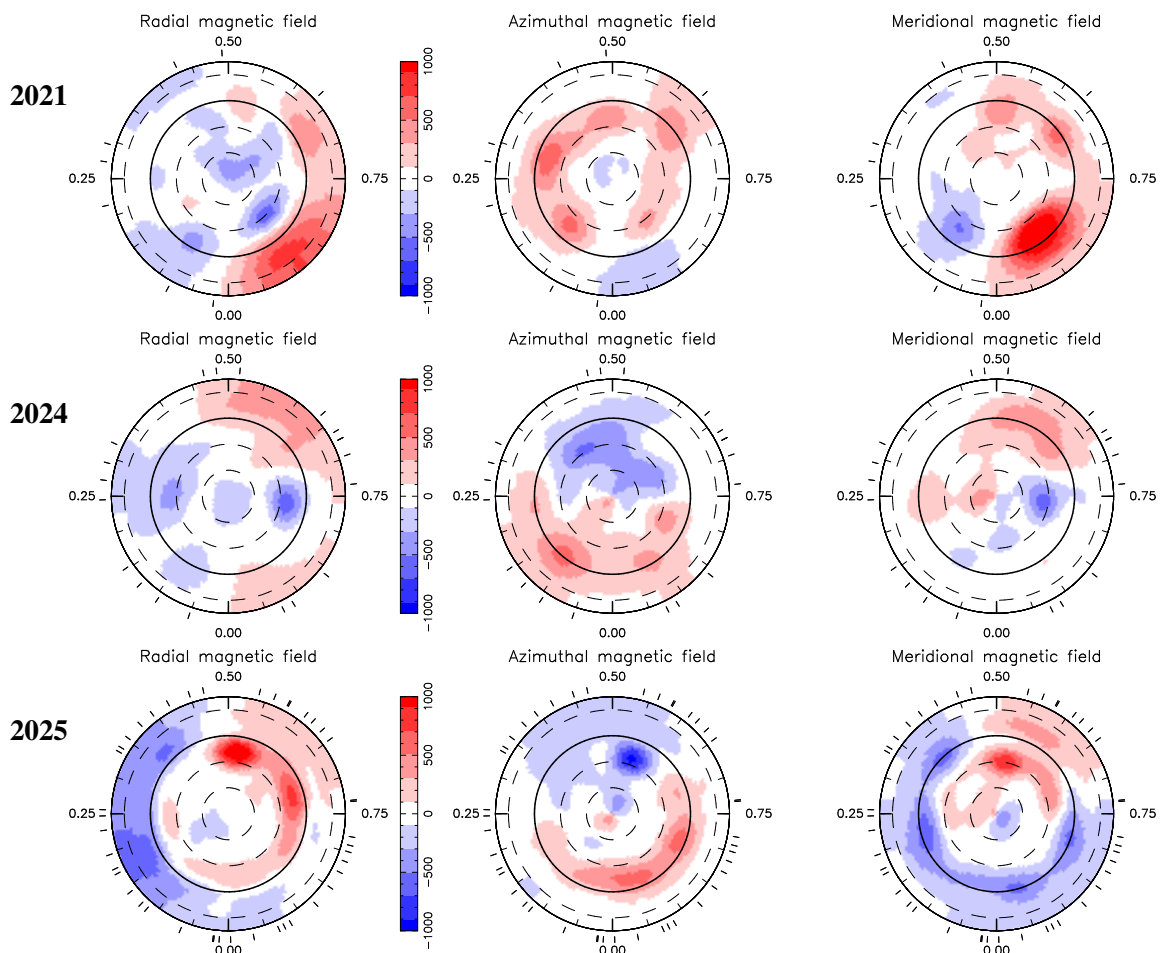


Fig. 3: Reconstructed maps of the large-scale field of DO Tau showing the radial, azimuthal and meridional components in spherical coordinates (left, middle and right columns, units in G), for seasons 2021, 2024, and 2025 (top to bottom rows, respectively). These maps, derived from the LSD Stokes I and V profiles of Fig. 2 using ZDI, are displayed in a flattened polar projection down to latitude -45° , with the north pole at the center and the equator depicted as a bold line. Outer ticks mark the phases of observations. Positive radial, azimuthal, and meridional fields point outward, counterclockwise, and poleward, respectively.

Table 3: Large-scale and small-scale fields measured from the magnetic topologies derived with ZDI in 2021, 2024, and 2025

Season	Stokes I & V analysis ($f_I = 0.9$, $f_V = 0.2$, $v_D = 3.0 \text{ km s}^{-1}$)					
	$\langle B_V \rangle$ (kG)	$\langle B_I \rangle$ (kG)	$\langle B_s \rangle$ (kG)	B_d (kG)	tilt / phase ($^\circ$)	pol/axi (%)
2021	0.39	1.8	1.4	-0.19	50 / 0.31	63 / 27
2024	0.30	1.4	1.4	-0.19	45 / 0.16	72 / 17
2025	0.40	1.8	1.5	0.32	66 / 0.68	76 / 34

Notes. Columns 2 and 3 list the quadratically averaged large-scale field ($\langle B_V \rangle$) and small-scale field ($\langle B_I \rangle$) over the stellar surface. Column 4 gives the time-averaged small-scale field integrated over the visible hemisphere ($\langle B_s \rangle$). Columns 5 to 7 list the polar strengths of the dipole component B_d , the tilt of the dipole component to the rotation axis and the phase toward which it is tilted, and the amount of magnetic energy reconstructed in the poloidal component of the field and in the axisymmetric modes of this component. Typical error bars on field values, percentages and dipole tilts are equal to 20%, 10%, and 10° in 2024 and 2025, and twice as much in 2021 due to the sparser sampling.

$f_I = 0.9$ (consistent with the results of ZeeTurbo; see Sec. 3) and $f_V = 0.2$, yielding optimal fits as for similar young stars (e.g., Donati et al. 2025b). Synthetic light curves were computed in the same way by summing the contributions of all visible cells,

estimated from their limb angle and reconstructed brightness at each rotation phase.

Figure 2 shows the ZDI fits to the LSD Stokes I and V profiles for each season, and Fig. 3 shows the corresponding reconstructed magnetic maps whose main characteristics are listed in Table 3. As a byproduct of the ZDI fit to the LSD Stokes profiles, we inferred that the rotational line broadening of DO Tau is equal to $v \sin i = 13.0 \pm 0.5 \text{ km s}^{-1}$ (in agreement with ZeeTurbo). The derived magnetic topology was mainly poloidal over the three seasons, with the dipole component encompassing 25–55% of the reconstructed poloidal field energy. The field was unusually complex for a young fully convective star, featuring in particular a mostly nonaxisymmetric poloidal component and a significant toroidal component. The only known cTTS with such a complex large-scale field is V2247 Oph (Donati et al. 2010). However, in contrast to DO Tau, V2247 Oph exhibited rapid temporal evolution and strong differential rotation, suggesting a different origin for its magnetic complexity. One option is that the strong accretion rate of DO Tau affects its inner convection pattern (Geroux et al. 2016) and the associated dynamo processes, leading to more complex magnetic fields. The large-scale field also evolved significantly from one season to the next, especially from 2024 to 2025, when the dipole component switched sign (as anticipated from the B_ℓ variations; see Sec. 4 and Table 3), a clear

difference with the large-scale fields of weakly accreting cTTSs (Zaire et al. 2024; Donati et al. 2024d,c). The small-scale field $\langle B_s \rangle$ of DO Tau inferred with ZDI (1.5 kG) remained stable throughout the campaign as did dT (see Sec. 4), a good proxy for $\langle B \rangle$ (Artigau et al. 2024; Cristofari et al. 2025). However, $\langle B_s \rangle$ is 40% smaller than $\langle B \rangle$ derived with ZeeTurbo (2.5 ± 0.3 kG) but still consistent with the estimate of López-Valdivia et al. (2021). The reconstructed field reached maximum strengths of 0.6 to 1.2 kG, consistent with the measurements of Dodin et al. (2013) at the funnel footpoints.

The brightness maps we simultaneously recovered with the magnetic maps all included a pair of bright and dark regions separated by about half a rotation cycle, directly reflecting the periodic distortions in the LSD Stokes I profiles causing the observed RV changes (see Fig. 2 and Sec. 6). Similar RV changes were also detected in the magnetically insensitive CO lines (see Sec. 6), demonstrating that these distortions are not caused by magnetic fields. However, the photometric curves predicted by ZDI featured a semi-amplitude (of 6–8%) larger than the observed fluctuations inferred from dT (see Fig. B.1). A tentative interpretation is that the LSD Stokes I profile distortions that ZDI interpreted as brightness spot signatures were actually caused by something else than temperature inhomogeneities, e.g., a corotating accretion funnel or a strong warp of the inner disk that regularly crossed and partially occulted the star, thereby generating no dT variations (as opposed to brightness spots).

6. RV modeling

As mentioned above, Stokes I LSD profiles of the atomic lines of DO Tau exhibited clear rotationally modulated distortions generating RV changes that ZDI interpreted as caused by brightness regions at the stellar surface. The bisector span (BIS) of the LSD profiles of atomic lines varied by about ± 1 km s $^{-1}$ (see Table A.1) and showed clear rotational modulation anticorrelated with RVs ($R \simeq -0.68$), further indicating that RV changes were mostly due to activity at the stellar surface (or to corotating occulting features in the inner disk). A similar behavior was observed in the CO lines. Modeling the RV activity jitter with QP GPR yielded semi-amplitudes θ_1 of $\simeq 0.9$ km s $^{-1}$ for LSD profiles of atomic and CO lines, and $\simeq 0.5$ km s $^{-1}$ for LBL RVs, with all three GP models varying in phase with one another (as expected since the three RV sets are strongly correlated). The derived period of the RV modulation, equal to 5.129 ± 0.003 d in all three cases, is fully consistent with that derived from B_ℓ (see Sec. 4).

To investigate whether DO Tau might host a massive planet in its close circumstellar environment, we also modeled RVs by adding a sine wave to describe the RV effect of a putative massive planet on a circular orbit in addition to the QP GP term describing activity. We studied the periodograms of the residuals of the activity-only GPR fit for the three sets of RVs and found that the LBL RVs exhibited the largest peaks at a period of 21.1 d and its most prominent one-month alias (66.5 d) with false-alarm probabilities (FAPs) of $\simeq 0.1\%$ (each peak surrounded by one-year aliases). The 21.1 d peak also dominated the residual periodogram of the RVs of the CO lines (but at a weaker level, with an FAP of a few percent and a one-month alias at 68.2 d), accompanied by another peak at 7.5 d. This is consistent with LBL RVs being dominated by information from molecular lines (including CO lines) in M stars. In contrast, the residual periodogram of RVs of the atomic lines instead showed a main peak at 15.6 d (again with an FAP of a few percent) plus a number of weaker peaks (including one at 21.1 d). That the RVs of atomic lines did not yield the same results as the other two RV

Table 4: MCMC results of the modeling of LBL RVs

Parameter	No planet	Planet b	Prior
θ_1 (km s $^{-1}$)	$0.50^{+0.13}_{-0.10}$	$0.53^{+0.13}_{-0.11}$	mod Jeffreys (σ_{RV})
θ_2 (d)	5.129 ± 0.003	5.130 ± 0.003	Gaussian (5.1; 0.3)
θ_3 (d)	600	600	fixed
θ_4	0.7	0.7	fixed
θ_5 (km s $^{-1}$)	0.21 ± 0.04	0.13 ± 0.04	mod Jeffreys (σ_{RV})
K_b (km s $^{-1}$)		0.22 ± 0.04	mod Jeffreys (σ_{RV})
P_b (d)		21.14 ± 0.02	Gaussian (21.1; 0.2)
T_b (2459000+)		1318.1 ± 0.6	Gaussian (1318; 5)
$M_b \sin i$ (M_{Jup})		2.0 ± 0.4	from K_b , P_b , M_\star
M_b (M_{Jup})		2.8 ± 0.6	assuming $i = 45^\circ$
a_b (au)		0.12 ± 0.01	
χ_r^2	1.71	1.07	
rms (km s $^{-1}$)	0.26	0.21	
$\log \mathcal{L}_M$	-28.1	-14.8	
$\Delta \log \mathcal{L}_M$	0.0	13.3	

Notes. We list the recovered GP and candidate planet parameters with their error bars, as well as the priors used where relevant, for the model without planet (column 2) and the best model with a candidate planet at 21.14 d (column 3). The last four rows report the χ_r^2 , the rms of the best fit to the RV data, the associated marginal logarithmic likelihood, $\log \mathcal{L}_M$, and the marginal logarithmic likelihood variation, $\Delta \log \mathcal{L}_M$, relative to the case without planet.

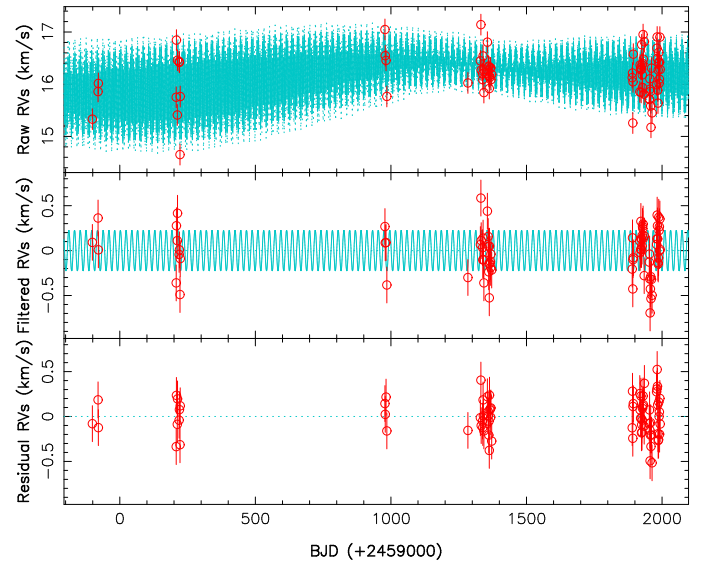


Fig. 4: Raw (top), filtered (middle), and residual (bottom) LBL RVs of DO Tau (red dots) over the observing period. The top panel shows the MCMC fit to the data, including a QP GPR modeling of the activity and a candidate planet on a 21.14 d circular orbit (cyan). The middle panel shows the planet RV signature (cyan) after activity was filtered out. The rms of the residuals is 0.21 km s $^{-1}$. A zoom-in on the 2025 data is shown in Fig. C.1.

sets suggests that these periodogram peaks might not be related to close-in planets (expected to affect all RV sets in an identical way) but rather to density structures in the inner accretion disk. We nonetheless explored the possibility that the main period in LBL RVs (at 21.1 d), also detected in RVs of CO lines, probes a candidate planet, to estimate its minimum mass in case it is real.

We achieved this by comparing the result of an MCMC fit to the LBL RVs with a model featuring a candidate planet and a QP GP describing activity, with that of a similar MCMC fit assuming no planet, the difference in $\log \mathcal{L}_M$ yielding the logarithmic

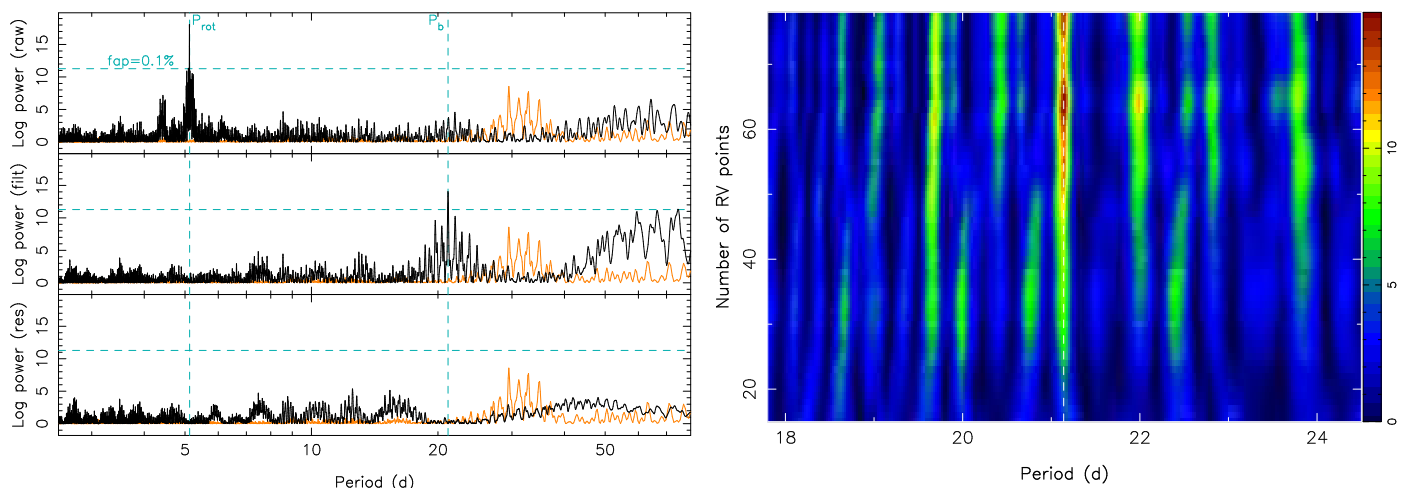


Fig. 5: Standard and stacked Lomb-Scargle periodograms of the RV data. Left panel: Periodogram of the raw (top), filtered (middle), and residual (bottom) LBL RV data, including a candidate planet on a 21.14 d circular orbit in the MCMC modeling. The dashed vertical cyan lines trace the stellar rotation period and the candidate planet orbital period, and the dashed horizontal lines indicate a 0.1% FAP level in the periodogram of the RV data. The orange curve depicts the periodogram of the window function. Right panel: Stacked periodograms of the filtered LBL RVs, as a function of the number of RV points included in the Fourier analysis. The color-scale indicates the logarithmic power in the periodogram. The vertical dashed line traces the candidate planet orbital period.

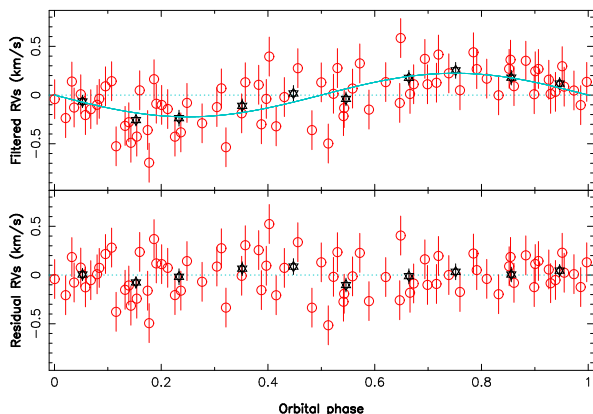


Fig. 6: Phase-folded filtered (top) and residual (bottom) LBL RVs for the model with a candidate planet on a 21.14 d circular orbit. The red dots show the measured RVs, and the black stars indicate average RVs over ten even phase bins.

Bayes factor in favor of the candidate planet. We found that the optimal orbital period was $P_b = 21.14 \pm 0.02$ d corresponding to an orbital distance of 0.12 ± 0.01 au, with a semi-amplitude of $K_p = 0.22 \pm 0.04$ km s $^{-1}$ indicating a minimum planet mass of $2.0 \pm 0.4 M_{\oplus}$ (planet mass of $2.8 \pm 0.6 M_{\oplus}$ assuming $i = 45^\circ$). The detected signal is apparently significant, with a logarithmic Bayes factor of $\Delta \log \mathcal{L}_M = 13.3$. Assuming that the candidate planet is on a Keplerian orbit yielded only a marginal improvement in $\log \mathcal{L}_M$ over the case with a circular orbit. The full result of the MCMC fit is outlined in Table 4 and the corresponding fit to the LBL RVs is shown in Fig. 4 (with a zoom-in on the 2025 data in Fig. C.1). The corresponding periodograms of the raw, filtered and residual LBL RVs are shown in the left panel of Fig. 5 where the peak at P_b features an FAP level of 0.006%. The stacked periodogram of the filtered RVs, displayed in the right panel of the same figure, exhibits a peak at P_b that strengthened irregularly as the number of points increased. This fluctuating peak strength might come from stochastic variability induced by

accretion; alternatively, it might reflect that the detected RV signal comes from activity associated with a variable disk structure and not from a candidate planet. The corresponding phase-folded filtered and residual RV curves are shown in Fig. 6.

Finally, we ran injection recovery tests to investigate the semi-amplitude threshold above which detections can be considered as reliable, for orbital periods of 6 to 100 d (see Fig. C.2). We found that, for periods in the range 8–25 d, $K_b \approx 0.23$ km s $^{-1}$ (corresponding to minimal masses of the candidate planet of 1.5 to 2.2 M_{\oplus}) is required on average to ensure a reliable detection with $\Delta \log \mathcal{L}_M = 10$. Beyond the drop in sensitivity for periods close to the synodic period of the Moon, the planet detectability weakens slightly, with $K_b \approx 0.25$ km s $^{-1}$ being required for a secure detection at an orbital period of 100 d (corresponding to a minimum mass 3.8 M_{\oplus}). This confirms that the candidate planet we identified is close to the detection threshold of our dataset.

7. Accretion and activity

The spectrum of DO Tau is subject to strong veiling, indicating high accretion rates at the surface of the star. We measured this veiling by comparing the equivalent widths (EW) of the LSD Stokes I profiles of DO Tau with those of the weak-line T Tauri stars TWA 25 and V819 Tau, whose spectral types are similar (as in Sousa et al. 2023). We obtained a first estimate, r_{JH} , from atomic lines (concentrating mostly in the JH band), and a second one, r_K , from the CO bandhead lines (redward of $2.28 \mu\text{m}$). The values we obtained, listed in Table A.1, range from 1.0 to 3.6 for r_{JH} (median 1.5), and from 1.6 to 6.1 for r_K (median 2.7). We found that r_K correlated well with r_{JH} ($R \approx 0.86$), with r_K being twice as large as r_{JH} on average. However, neither r_{JH} nor r_K showed rotational modulation, each exhibiting various peaks in the periodogram (including one at ≈ 21 d).

We also examined the 1083 nm He I triplet and constructed the 2D periodograms of its profile for seasons 2024 and 2025 (see Fig. 7). The line profile featured redshifted emission associated with accretion processes (extending to 250 km s $^{-1}$) as well as blueshifted absorption and emission probing the stellar and disk winds (extending to -250 km s $^{-1}$). It also featured red-

shifted absorption (between 50 and 200 km s⁻¹) tracing accretion funnels or strong warps in the inner accretion disk regularly crossing the line of sight. Rotational modulation was detected in the central emission peak, possibly related to chromospheric emission (as in PDS 70, Donati et al. 2024a); in 2025, rotational modulation was also observed in the redshifted absorption. In the blueshifted component probing the stellar and disk winds, longer periods, ranging from 13 d (in 2024 and 2025) to ≈ 16 d (in 2025 only), were also observed at low velocities, suggesting transient phenomena occurring at the base of the wind every few stellar rotation cycles. In 2025, i.e., the season for which our dataset was most extended, the 2D periodogram rapidly evolved with time, with the blueshifted component showing a period of ≈ 17 d in the first half of the dataset, then clear rotational modulation in the second half (see Fig. D.2). Rapid evolution was likely also at work in previous epochs.

We similarly investigated the 1282 nm Pa β and 2166 nm Br γ lines, whose profiles and 2D periodograms for seasons 2024 and 2025 are shown in Figs. 8 and D.1. Both lines exhibited similar patterns, Br γ being weaker and more noisy than Pa β . The blueshifted half of both lines showed periods similar to those seen in the blue wing of He I, suggesting that it is also associated with winds from the star and the disk; the redshifted absorption of Pa β and Br γ , probing funnel or inner disk material crossing the line of sight, showed conspicuous rotational modulation from velocities 50 to 200 km s⁻¹ in 2024, but only up to 150 km s⁻¹ and occurring at lower velocities in Br γ than in Pa β in 2025. As for He I, the 2D periodograms of both lines evolved with time in 2025, showing both 11 and 16 d periods in the blueshifted half of the profile in the first half of the season, then no periodicity in the second half. Similarly, rotational modulation of the redshifted absorption, obvious in the first half of the season, vanished almost completely in the second half (see Figs. D.3 and D.4). This suggests that unstable accretion occurred at the stellar surface from the inner accretion disk.

By summing the 50–200 km s⁻¹ spectral bins of each line, we obtained fluxes that are rotationally modulated, more clearly for Br γ than for Pa β but nonetheless well correlated with one another ($R \approx 0.75$). Though noisier than Pa β , Br γ was less subject to accretion-related stochastic variations, and exhibited cleaner rotational modulation of the redshifted absorption. A GPR fit to these fluxes (with θ_3 and θ_4 fixed to 600 and 0.7 as in Table 4) yielded period estimates of 5.10 ± 0.05 d for both lines, consistent with our determination of P_{rot} within the error bars. Maximum redshifted absorption in Pa β and Br γ , signaling the phase at which the absorbing material crossed the line of sight, occurred at phases 0.80–0.90 in 2021, 0.15–0.25 in 2024, and 0.40–0.50 in 2025. In 2024, this phase roughly coincided with the phase toward which the reconstructed dipole component was tilted (0.16; see Table 3) and with the bright region reconstructed with ZDI (see Fig. B.1), implying that the redshifted absorption was likely caused by the main accretion funnel crossing the line of sight. The bright photospheric region might have reflected the hot chromospheric spot, although dT did not show a maximum at this phase (see Fig. B.1). In 2021, in contrast, the phase of maximum Pa β and Br γ redshifted absorption occurred about half a rotation cycle later than the phase toward which the inferred dipole component was tilted (0.31; see Table 3), as if the accretion funnel crossing the line of sight was now connected to the positive (rather than negative) pole of the dipole. It also coincided with the dark (rather than the bright) region reconstructed with ZDI (see Fig. B.1). In 2025, finally, maximum Pa β and Br γ redshifted absorption occurred roughly at mid distance between the crossing of the negative and positive poles (located

close to the equator at phases 0.18 and 0.68, respectively; see Fig. 3), and matched the dark spot reconstructed with ZDI (see Fig. B.1), suggesting this time that it might probe a strong warp of the inner disk.

We computed the emission EWs for Pa β and Br γ (see Table A.1) and found that they correlated with veiling r_{JH} and r_K ($R \approx 0.7$ and 0.6 for Pa β and Br γ , respectively). We also found that Pa β and Br γ EWs were strongly correlated with one another ($R \approx 0.95$), with Pa β EWs being stronger than Br γ ones by an average factor of 4.2 (2.7 after correcting for veiling). We then used the scaling relations of Fiorellino et al. (2025) and our stellar parameters (see Table 1) to turn the veiling-corrected EWs of Pa β and Br γ into accretion fluxes and the logarithmic mass-accretion rates $\log \dot{M}$ for each visit. We derived time-averaged values of -7.72 ± 0.24 dex (\dot{M} in $M_{\odot} \text{ yr}^{-1}$) for Pa β and -7.78 ± 0.31 dex for Br γ , the error bar denoting the dispersion over all visits. Taking the weighted average of both estimates yielded $\log \dot{M} = -7.74 \pm 0.19$ dex, consistent with previous results (Alcalá et al. 2021; Sousa et al. 2023; Perraut et al. 2025). We found for individual seasons that DO Tau accreted mass marginally faster in 2021 ($\log \dot{M} = -7.47 \pm 0.15$ dex) and in 2024 (-7.65 ± 0.14 dex) than in 2025 (-7.87 ± 0.16 dex), without a clear variation between the first and second half of the 2025 season. From the average mass-accretion rate, the intensity of the reconstructed dipole component of the large-scale field (0.20–0.30 kG; see Table 3) and the stellar parameters of Table 1, we derive following Bessolaz et al. (2008), that the magnetospheric gap of DO Tau extended to a distance of $r_{\text{mag}} = 1.6 \pm 0.3 R_{\star}$ or 0.014 ± 0.002 au (the error bar corresponding to variations in the dipole field strength and the mass accretion rate), implying that $r_{\text{mag}}/r_{\text{cor}} = 0.30 \pm 0.05$ where r_{cor} denotes the corotation radius (located at $5.4 R_{\star}$, i.e., 0.047 au) at which the Keplerian angular velocity equals the rotation rate at the stellar surface. Our r_{mag} estimate is consistent with that inferred with Gravity from the size of the Br γ emitting region (Perraut et al. 2025).

In this regime and following Blinova et al. (2016), magnetospheric accretion is expected to be unstable but ordered, with one to two tongues of accreted material penetrating the magnetosphere in the equatorial plane. For an inclined dipole, accretion at the surface of the star is expected to be rotationally modulated and to fluctuate with the Keplerian period of the inner disk (0.84 d), generating rapid intrinsic variability in addition to rotational modulation¹. This is qualitatively consistent with what we observed, with maximum redshifted absorption occurring in conjunction with either poles of the magnetic dipole in 2021 and 2024. For dipoles that are strongly tilted to the rotation axis (as in 2025), magnetospheric accretion is predicted to proceed directly to the magnetic poles in the equatorial plane and to generate a strong warp in the inner disk at mid distance from magnetic poles (Romanova et al. 2003). We speculate that this strong warp generated the periodic distortions in Stokes I profiles and redshifted absorption in emission lines in 2025. The disk warp material, located well within the corotation radius and forced to corotate with the star, was unable to escape falling toward the star, albeit at reduced speed given the transverse orientation of the magnetic field. This makes our observations qualitatively consistent with theoretical expectations. Given the low r_{mag} , we also expect the higher SH terms of the magnetic topology to contribute to rendering the accretion pattern more complex and unstable. The large-scale field of DO Tau is likely too weak to prevent accretion of angular momentum from the disk,

¹ Periodograms of the TESS light curves also show peaks at periods shorter than P_{rot} down to about ≈ 1 d, in line with model predictions.

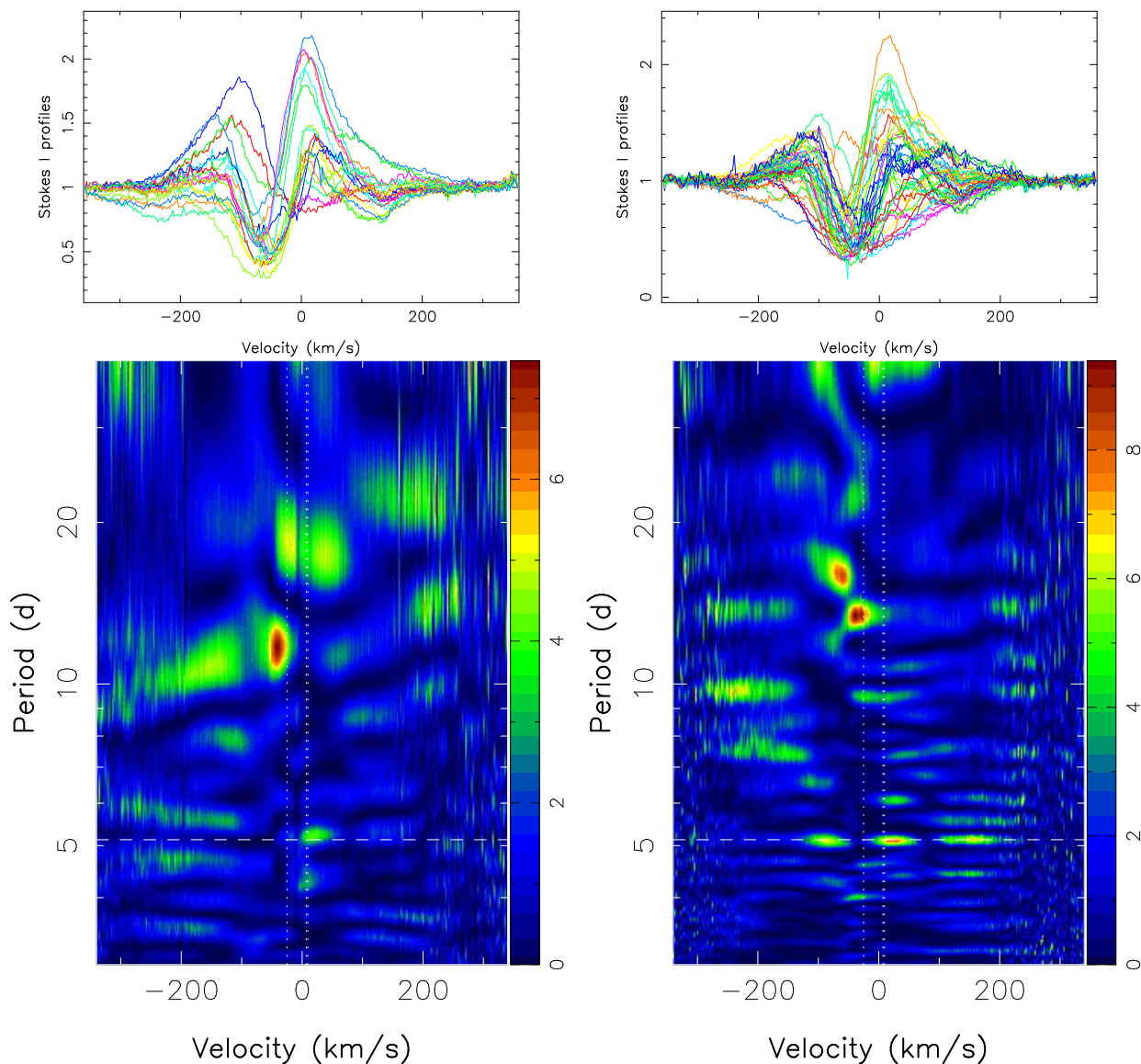


Fig. 7: Stacked Stokes I profiles (top plots) and 2D periodograms (bottom plots) of the 1083.3 nm He I IRT in the stellar rest frame for seasons 2024 (left panels) and 2025 (right panels). The dashed horizontal line traces P_{rot} and the vertical dotted lines depict the velocities of the three components of the He I triplet. The color-scale traces the logarithmic power in the periodogram. Only the main peaks (yellow to red and extending over at least several velocity bins) are likely to be significant.

causing the star to speed up, in contrast to more slowly rotating cTTSs with stronger fields and lower accretion rates (like CI Tau, Donati et al. 2024d).

We also studied the [Fe II] J and H and H₂ lines (at 1257.02, 1644.00, and 2121.83 nm), which probe the jet and outflow of DO Tau (Erkal et al. 2021) and were found to vary very weakly. We report a $\approx 1 \text{ km s}^{-1}$ shift of the [Fe II] lines from 2024 to 2025.

8. Summary

We carried out a spectropolarimetric study of DO Tau based on 77 SPIRou Stokes I and V spectra collected from early 2020 to late 2025. From the detected Zeeman polarization signatures in LSD profiles of atomic lines, we infer that DO Tau rotates in $P_{\text{rot}} = 5.128 \pm 0.002 \text{ d}$, with its rotation axis inclined at $45 \pm 8^\circ$ to the line of sight, slightly more than the outer accretion disk. The rotational broadening of spectral lines, $v \sin i = 13.0 \pm 0.5 \text{ km s}^{-1}$, implied that DO Tau has a radius of $R_\star = 1.9 \pm 0.2 R_\odot$. The

atmospheric parameters derived with ZeeTurbo, $T_{\text{eff}} = 3450 \pm 50 \text{ K}$ and $\log g = 3.6 \pm 0.1$, suggest that DO Tau is still fully convective, with an age of $1.7 \pm 0.5 \text{ Myr}$.

We found that the average large-scale and small-scale magnetic field strengths at the surface of DO Tau were equal to 0.35 and 2.5 kG, respectively. The large-scale field reconstructed with ZDI was mostly nonaxisymmetric and featured a significant toroidal component. The dipole component of the poloidal field, ranging from 0.2 to 0.3 kG, became more inclined with respect to the rotation axis, with the negative pole eventually changing hemisphere between the last two seasons. If this is confirmed, DO Tau is the first cTTS for which a global polarity switch of the large-scale magnetic field is detected, bringing further evidence that large-scale magnetic fields of cTTSs are dynamo amplified rather than fossil fields. The large-scale field of DO Tau was unusually weak and complex for a cTTS (see Fig. 9). DO Tau even differs from its closest cTTS neighbor in our Hertzsprung-Russel diagram, V2247 Oph, whose complex field varied very rapidly

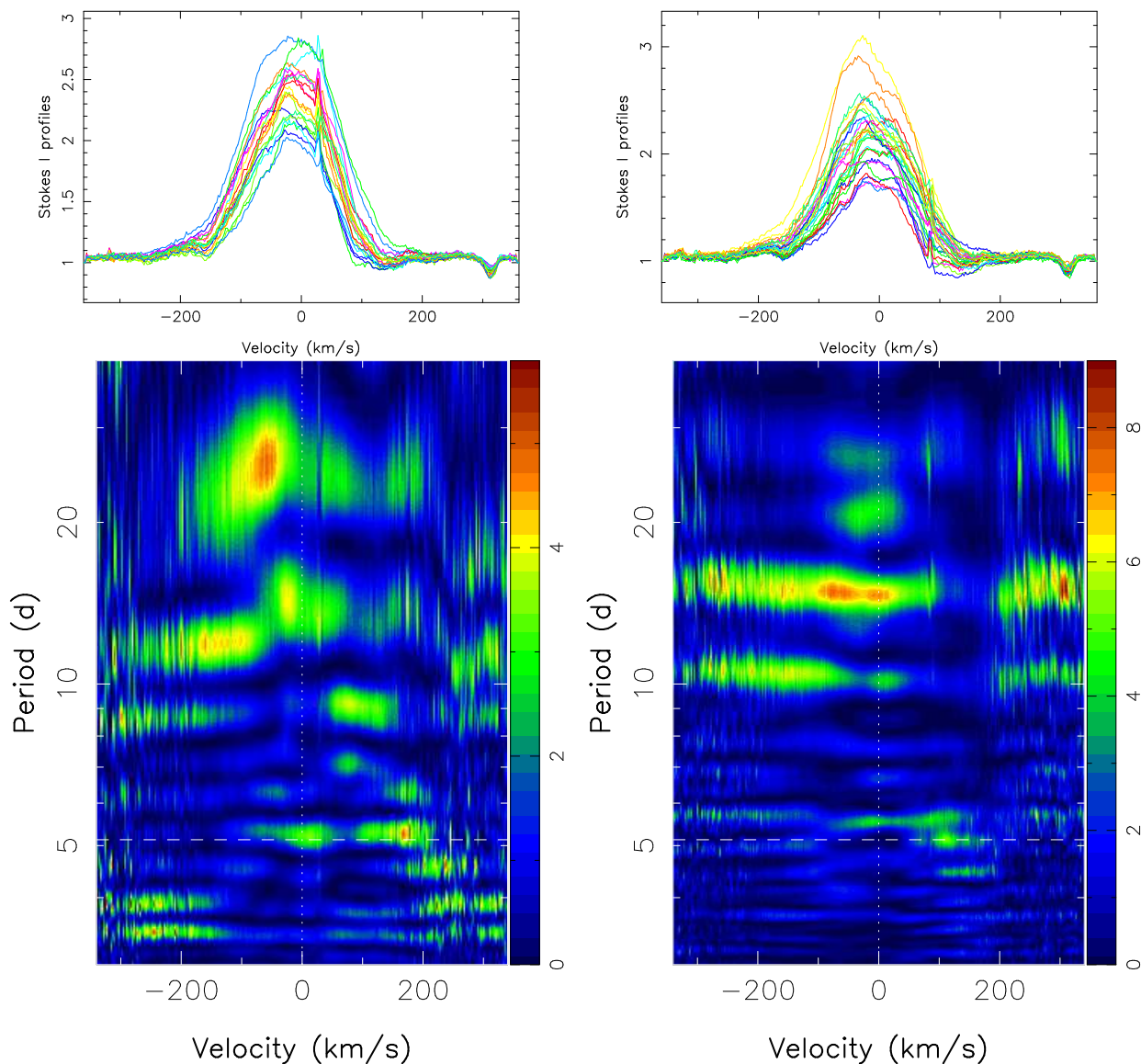


Fig. 8: Same as Fig. 7 for the 1282 nm Pa β line (left: 2024, right: 2025).

under strong differential rotation (Donati et al. 2010). This difference might be caused by intense accretion from the inner disk that affects convection and dynamo action (Geroux et al. 2016).

Strong and variable veiling and fluxes in emission lines were detected at all times and were well correlated, but showed no rotational modulation, emphasizing the stochastic nature of accretion from the inner disk. The average logarithmic mass-accretion rate derived from veiling-corrected Pa β and Bry fluxes was equal to $\log \dot{M} = -7.74 \pm 0.19$ dex, marginally stronger in 2021 and 2024 than in 2025. The magnetospheric radius we derived from the large-scale dipole, the mass accretion rate and the stellar parameters is equal to $1.6 \pm 0.3 R_{\star}$ or $0.30 \pm 0.05 r_{\text{cor}}$, suggesting that accretion is complex and unstable on DO Tau, occurring via a few tongues penetrating the magnetosphere in the equatorial plane. The redshifted absorption in Pa β and Bry, most of the time modulated by rotation, was interpreted as due to accretion funnels linking the inner disk to one of the magnetic poles and regularly crossing the line of sight. In 2025, however, this redshifted absorption was instead attributable to a warp in the inner accretion disk likely induced by the strongly tilted magnetosphere. Stellar and disk wind signatures were also detected

in the blue wings of the He I triplet, Pa β and Bry, with periods varying between 13 and 16 d from one season to the next, presumably reflecting sporadic events induced by accretion bursts; rotational modulation of the He I wind signatures was also observed in the second half of the 2025 season.

The RVs of DO Tau, either measured with LBL on all lines or on LSD profiles of atomic and CO lines, also varied, reflecting mainly rotational modulation caused by activity. We report a potential RV contribution from a candidate massive planet orbiting within the inner disk at a distance of 0.12 ± 0.01 au (orbital period $P_b = 21.14 \pm 0.02$ d). The detected RV signature, best seen in LBL RVs and in CO lines but only marginally in atomic lines, featured a semi-amplitude of $K_b = 0.22 \pm 0.04$ km s $^{-1}$, would imply a minimum mass of $2.0 \pm 0.4 M_{\text{J}}$ for the candidate planet, i.e., a mass of $2.8 \pm 0.6 M_{\text{J}}$ if the orbital motion takes place in the stellar equatorial plane. The observed RV signal is close to the detection threshold of our dataset according to planet injection recovery tests, however. Moreover, the three RV sets yielded differing periodograms, and the veiling also showed some power at 21 d, which might suggest that the reported RV

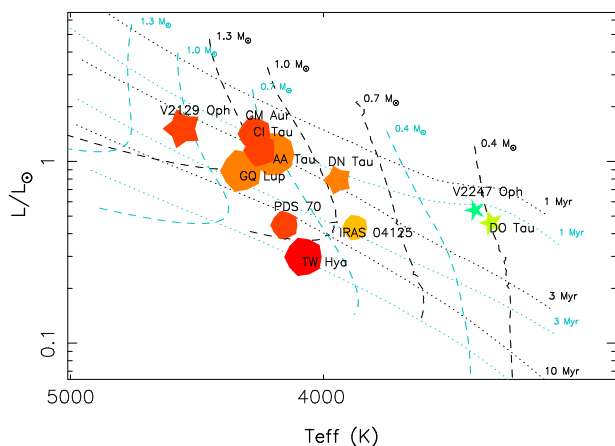


Fig. 9: Basic properties of the large-scale magnetic topologies of cTTSs, as a function of their locations in the Hertzsprung-Russell diagram. The symbol size indicates relative magnetic intensities, the symbol colour illustrates the field configurations (red to blue for purely poloidal to purely toroidal fields), and the symbol shape depicts the degree of axisymmetry of the poloidal field component (decagon and stars for purely axisymmetric and purely nonaxisymmetric poloidal fields, respectively). We also show the most recent magnetic (black) and nonmagnetic (cyan) PMS evolutionary tracks (dashed lines) and isochrones (dotted lines) of Feiden (2016).

signature comes from activity related to a density structure in the inner disk and not from a close-in planet.

Our spectropolarimetric and velocimetric study of DO Tau showed that collecting both types of data is essential for characterizing the physical processes taking place in the close environments of young cTTSs, especially those featuring strong accretion rates. For instance, work like this can test the tentative scenarios invoked to explain the wiggle of the jet axis (Erkal et al. 2021), i.e., a warp induced by a magnetic disk wind or a slightly inclined close-in massive planet. If this is confirmed, the candidate planet is less massive than required ($6\text{--}12 M_{\oplus}$), but in the correct range of orbital distances ($0.10\text{--}0.15$ au) and on a possibly inclined orbit given the misalignment of the inner and outer disks. In addition, the variable stellar magnetic field switching polarity might be an alternative option for generating warps in the inner disk. Follow-up monitoring of DO Tau simultaneously with SPIROU and ESPaDOnS at optical and nIR wavelengths (i.e., with VISION, to be commissioned at the CFHT in 2026) and complementary instruments should reveal which of these options explains the observations best. It will also further document the temporal evolution of the large-scale magnetic field of DO Tau and its possible cyclic variations, clarify the effect of strong accretion on the dynamo processes and the dynamics of convective zones in young low-mass stars, and ultimately improve physical realism in models of star and planet formation.

Data availability

SPIROU data used in this study are, or will soon be, publicly available at the Canadian Astronomy Data Center (<https://www.cadc-ccda.hia-ihp.nrc-cnrc.gc.ca>).

Acknowledgements. We thank an anonymous referee for constructive comments that improved the paper. This work benefited from the SIMBAD CDS database at URL <http://simbad.u-strasbg.fr/simbad> and the ADS system at URL <https://ui.adsabs.harvard.edu>. We thank Dr Greg Feiden for providing us the tracks and isochrones of his latest magnetic and non-magnetic stellar

evolution models. Our study is based on data obtained at the CFHT, operated by the CNRC (Canada), INSU/CNRS (France) and the University of Hawaii. The authors wish to recognise and acknowledge the very significant cultural role and reverence that the summit of Maunakea has always had within the indigenous Hawaiian community. SHPA acknowledges financial support from CNPq, CAPES and Fapemig. FM received funding from the European Research Council (ERC) under the European Union's Horizon Europe research and innovation program (grant agreement #101053020 Dust2Planets).

References

- Alcalá, J. M., Gangi, M., Biazzo, K., et al. 2021, *A&A*, 652, A72
Alcalá, J. M., Manara, C. F., Natta, A., et al. 2017, *A&A*, 600, A20
Amard, L. & Matt, S. P. 2023, *A&A*, 678, A7
Armeni, A., Stelzer, B., Frasca, A., et al. 2024, *A&A*, 690, A225
Artigau, E., Cadieux, C., Cook, N. J., et al. 2024, *AJ*, 168, 252
Artigau, E., Cadieux, C., Cook, N. J., et al. 2022, *AJ*, 164, 84
Baraffe, I., Homeier, D., Allard, F., & Chabrier, G. 2015, *A&A*, 577, A42
Barber, M. G., Mann, A. W., Vanderburg, A., et al. 2024, *Nature*, 635, 574
Bessolaz, N., Zanni, C., Ferreira, J., Keppens, R., & Bouvier, J. 2008, *A&A*, 478, 155
Blinova, A. A., Romanova, M. M., & Lovelace, R. V. E. 2016, *MNRAS*, 459, 2354
Braun, T. A. M., Yen, H.-W., Koch, P. M., et al. 2021, *ApJ*, 908, 46
Chib, S. & Jeliakzov, I. 2001, *Journal of the American Statistical Association*, 96, 270
Cody, A. M., Hillenbrand, L. A., & Rebull, L. M. 2022, *AJ*, 163, 212
Cook, N. J., Artigau, E., Doyon, R., et al. 2022, *PASP*, 134, 114509
Cristofari, P. I., Donati, J.-F., Bellotti, S., et al. 2025, *A&A*, 702, A111
Cristofari, P. I., Donati, J. F., Folsom, C. P., et al. 2023, *MNRAS*, 522, 1342
Dodin, A. V., Lamzin, S. A., & Chuntunov, G. A. 2013, *Astrophysical Bulletin*, 68, 177
Donati, J., Skelly, M. B., Bouvier, J., et al. 2010, *MNRAS*, 402, 1426
Donati, J. F., Cristofari, P. I., Alencar, S. H. P., et al. 2024a, *MNRAS*, 535, 3363
Donati, J. F., Cristofari, P. I., Carmona, A., & Grankin, K. 2024b, *MNRAS*, 534, 231
Donati, J. F., Cristofari, P. I., Finocciety, B., et al. 2023, *MNRAS*, 525, 455
Donati, J. F., Cristofari, P. I., Klein, B., Finocciety, B., & Moutou, C. 2025a, *A&A*, 700, A122
Donati, J. F., Cristofari, P. I., Lehmann, L. T., et al. 2024c, *MNRAS*, 531, 3256
Donati, J. F., Finocciety, B., Cristofari, P. I., et al. 2024d, *MNRAS*, 530, 264
Donati, J. F., Gaidos, E., Moutou, C., et al. 2025b, *A&A*, 698, L14
Donati, J.-F., Howarth, I. D., Jardine, M. M., et al. 2006, *MNRAS*, 370, 629
Donati, J. F., Kouch, D., Moutou, C., et al. 2020, *MNRAS*, 498, 5684
Donati, J.-F., Semel, M., Carter, B. D., Rees, D. E., & Collier Cameron, A. 1997, *MNRAS*, 291, 658
Erkal, J., Dougados, C., Coffey, D., et al. 2021, *A&A*, 650, A46
Feiden, G. A. 2016, *A&A*, 593, A99
Fernández-López, M., Zapata, L. A., Rodríguez, L. F., et al. 2020, *AJ*, 159, 171
Finocciety, B. & Donati, J. F. 2022, *MNRAS*, 516, 5887
Fiorellino, E., Alcalá, J. M., Manara, C. F., et al. 2025, *A&A*, 704, A42
Fischer, W. J., Hillenbrand, L. A., Herczeg, G. J., et al. 2023, in *Astronomical Society of the Pacific Conference Series*, Vol. 534, *Protostars and Planets VII*, ed. S. Inutsuka, Y. Aikawa, T. Muto, K. Tomida, & M. Tamura, 355
Gaia Collaboration. 2020, *VizieR Online Data Catalog: Gaia EDR3 (Gaia Collaboration, 2020)*, *VizieR On-line Data Catalog: I/350*. Originally published in: 2021A&A...649A...1G
Geroux, C., Baraffe, I., Viallet, M., et al. 2016, *A&A*, 588, A85
Haywood, R. D., Collier Cameron, A., Queloz, D., et al. 2014, *MNRAS*, 443, 2517
Huang, J., Ginski, C., Benisty, M., et al. 2022, *ApJ*, 930, 171
Krolikowski, D. M., Kraus, A. L., & Rizzuto, A. C. 2021, *AJ*, 162, 110
Landi degl'Innocenti, E. & Landolfi, M. 2004, *Polarisation in spectral lines (Dordrecht/Boston/London: Kluwer Academic Publishers)*
Lehmann, L. T. & Donati, J. F. 2022, *MNRAS*, 514, 2333
Long, F., Herczeg, G. J., Harsono, D., et al. 2019, *ApJ*, 882, 49
López-Valdivia, R., Sokal, K. R., Mace, G. N., et al. 2021, *ApJ*, 921, 53
Pérez Paolino, F., Bary, J. S., Hillenbrand, L. A., Markham, M., & Fischer, W. J. 2025, *ApJ*, 978, 32
Perraut, K., Bouvier, J., Nowacki, H., et al. 2025, *A&A*, in press
Rajpaul, V., Aigrain, S., Osborne, M. A., Reece, S., & Roberts, S. 2015, *MNRAS*, 452, 2269
Rescigno, F., Mortier, A., Dumusque, X., et al. 2024, *MNRAS*, 532, 2741
Romanova, M. M., Espaillat, C. C., Wendeborn, J., et al. 2025, *MNRAS*, 538, 480
Romanova, M. M., Koldoba, A. V., Ustyugova, G. V., et al. 2021, *MNRAS*, 506, 372
Romanova, M. M., Koldoba, A. V., Ustyugova, G. V., Espaillat, C. C., & Lovelace, R. V. E. 2026, *MNRAS[arXiv:2507.15115]*
Romanova, M. M., Ustyugova, G. V., Koldoba, A. V., Wick, J. V., & Lovelace, R. V. E. 2003, *ApJ*, 595, 1009
Ryabchikova, T., Piskunov, N., Kurucz, R. L., et al. 2015, *Phys. Scr*, 90, 054005
Skillington, J. & Bryan, R. K. 1984, *MNRAS*, 211, 111
Sousa, A. P., Bouvier, J., Alencar, S. H. P., et al. 2023, *A&A*, 670, A142
Winter, A. J., Booth, R. A., & Clarke, C. J. 2018, *MNRAS*, 479, 5522
Zaire, B., Donati, J.-F., Alencar, S. P., et al. 2024, *MNRAS*, 533, 2893

Appendix A: SPIRou observations: additional material

Table A.1 provides the observation log for the SPIRou spectra of DO Tau, and the measurements derived from them at each epoch.

Appendix B: ZDI modeling: Additional material

Figure B.1 shows, for each season, the brightness maps derived simultaneously with the magnetic maps of Fig. 3 and the corresponding photometric light curves compared to those derived from dT .

Appendix C: RV modeling: Additional material

Figure C.1 shows the RV curve and MCMC + GPR fit, zooming-in on the 2025 data. Figure C.2 shows the detectability of RV signatures as a function of orbital period for our DO Tau RV data.

Appendix D: Accretion and activity: Additional material

Figure D.1 shows the 2D periodogram of the Bry line in season 2024 and 2025. Figures D.2, D.3, and D.4 show similar plots for the first and second half of the 2025 season, for the He I, Pa β , and Bry lines.

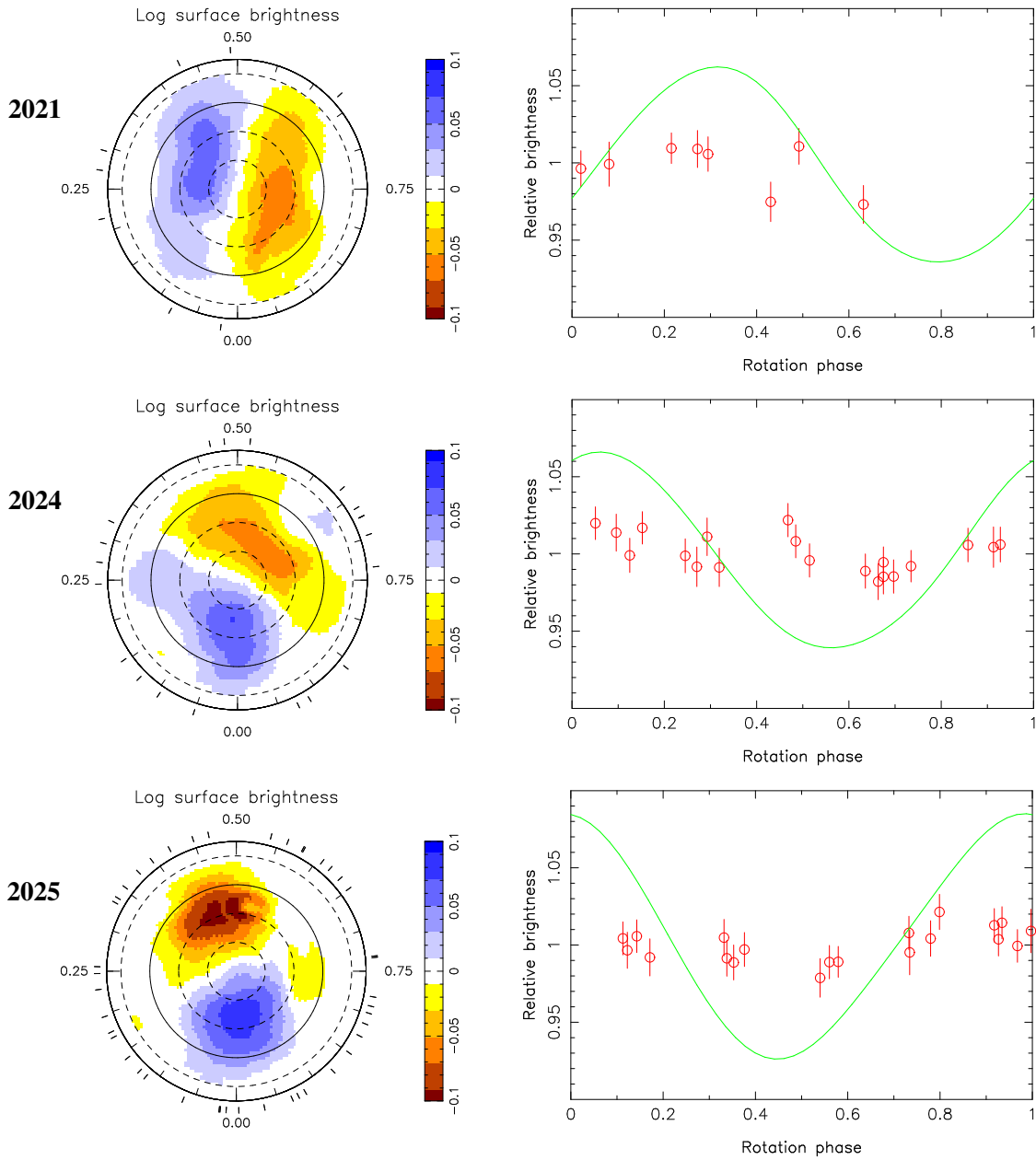


Fig. B.1: Maps of the logarithmic relative surface brightness (with respect to the quiet photosphere, left panels) reconstructed simultaneously with the magnetic maps of Fig. 3 with ZDI from the LSD Stokes I and V profiles of Fig. 2, and corresponding photometric light curves (right panels, green curves) along with estimates inferred from dT measurements (assuming a blackbody at photospheric temperature, red circles). In the brightness maps, yellow and blue depict regions darker and brighter than the quiet photosphere, respectively.

Table A.1: Observing log of our SPIRou observations of DO Tau

BJD (2459000+)	UT date	BERV (km s ⁻¹)	c / ϕ	t _{exp} (s)	S/N (H)	σ_p (10 ⁻⁴ I _c)	LBL RV (km s ⁻¹)	B _l (G)	BIS (km s ⁻¹)	r _{JH} / r _K	EW Pa β / Bry (km s ⁻¹)
-101.200530	19 Feb 2020	-29.541	0 / 0.019	1582.4	249	2.09	15.33±0.20	-55±28	1.7±0.4	2.95 / 4.08	221 / 38.6
-80.200386	11 Mar 2020	-29.896	4 / 0.115	1582.4	220	2.64	15.86±0.20	-118±22	0.8±0.3	1.42 / 2.17	143 / 14.7
-79.259681	12 Mar 2020	-29.712	4 / 0.298	1582.4	235	2.26	16.02±0.20	-108±19	0.2±0.3	1.54 / 2.59	162 / 24.2
207.891658	24 Dec 2020	-10.968	60 / 0.295	1604.7	316	1.82	15.75±0.20	-57±21	-0.3±0.3	2.48 / 4.00	333 / 74.4
208.902257	25 Dec 2020	-11.495	60 / 0.492	1604.7	290	1.98	16.85±0.20	-54±26	-0.8±0.3	2.88 / 4.50	454 / 85.1
211.920555	28 Dec 2020	-13.012	61 / 0.080	1604.7	205	2.93	15.41±0.20	20±26	0.2±0.3	1.62 / 2.85	260 / 48.2
212.902188	29 Dec 2020	-13.441	61 / 0.272	1604.7	235	2.51	16.46±0.20	-44±25	-0.8±0.3	1.92 / 3.06	306 / 61.3
218.843346	04 Jan 2021	-16.073	62 / 0.430	1604.7	261	2.18	16.43±0.20	-71±17	-0.9±0.3	1.32 / 1.70	262 / 43.6
219.874312	05 Jan 2021	-16.615	62 / 0.631	1604.7	247	2.26	16.42±0.20	21±18	-0.5±0.3	1.32 / 2.11	216 / 30.1
221.862565	07 Jan 2021	-17.472	63 / 0.019	1604.7	232	2.42	14.65±0.20	-8±26	0.4±0.3	2.17 / 3.00	253 / 51.7
222.868775	08 Jan 2021	-17.928	63 / 0.215	1604.7	285	1.87	15.76±0.20	-31±21	-0.0±0.3	2.35 / 4.92	312 / 58.5
977.892123	02 Feb 2023	-26.588	210 / 0.451	1627.0	296	1.83	17.05±0.20	-32±23	-1.4±0.3	2.76 / 4.64	276 / 46.7
978.910461	03 Feb 2023	-26.872	210 / 0.649	1627.0	256	2.10	16.55±0.20	151±27	-0.3±0.3	2.80 / 4.76	268 / 38.4
981.883376	06 Feb 2023	-27.531	211 / 0.229	1627.0	278	1.94	16.46±0.20	-130±30	0.5±0.2	3.52 / 5.41	315 / 61.4
1329.903770	20 Jan 2024	-22.495	279 / 0.096	1627.0	269	2.06	16.45±0.20	-41±19	0.4±0.3	1.76 / 4.10	268 / 44.6
1331.812171	22 Jan 2024	-22.959	279 / 0.468	1627.0	321	1.60	17.14±0.20	18±25	-1.4±0.5	3.62 / 6.14	350 / 67.3
1332.871797	23 Jan 2024	-23.461	279 / 0.675	1627.0	286	1.82	16.27±0.20	95±20	1.0±0.3	2.29 / 4.30	329 / 58.5
1337.941736	28 Jan 2024	-25.196	280 / 0.663	1627.0	258	2.07	16.20±0.20	106±17	1.1±0.3	1.47 / 3.09	202 / 32.3
1338.939065	29 Jan 2024	-25.488	280 / 0.858	1627.0	246	2.12	16.09±0.20	33±20	0.8±0.3	1.86 / 4.24	212 / 31.9
1339.928170	30 Jan 2024	-25.758	281 / 0.051	1627.0	284	1.85	16.54±0.20	-7±19	-0.4±0.3	2.08 / 4.64	201 / 28.1
1340.926524	31 Jan 2024	-26.036	281 / 0.245	1627.0	279	1.84	16.28±0.20	-154±15	-0.7±0.3	1.49 / 3.06	136 / 21.0
1342.927215	02 Feb 2024	-26.575	281 / 0.636	1627.0	248	2.11	15.84±0.20	126±22	1.0±0.3	2.10 / 3.78	231 / 36.9
1355.833637	15 Feb 2024	-29.084	284 / 0.152	1627.0	301	1.71	16.81±0.20	-105±19	1.0±0.3	2.26 / 4.59	218 / 35.6
1358.818568	18 Feb 2024	-29.453	284 / 0.735	1627.0	284	1.81	16.26±0.20	58±17	1.2±0.4	1.80 / 3.43	286 / 46.4
1359.810746	19 Feb 2024	-29.553	284 / 0.928	1627.0	258	1.99	16.34±0.20	8±19	1.2±0.3	1.89 / 3.44	264 / 39.9
1360.821815	20 Feb 2024	-29.682	285 / 0.125	1627.0	269	1.97	16.15±0.20	-133±15	-0.1±0.3	1.26 / 2.66	231 / 35.7
1361.816345	21 Feb 2024	-29.768	285 / 0.319	1627.0	246	2.16	16.33±0.20	-187±17	-0.8±0.3	1.28 / 2.58	180 / 30.6
1362.818972	22 Feb 2024	-29.863	285 / 0.515	1627.0	274	1.91	15.92±0.20	35±19	1.0±0.3	1.89 / 4.16	221 / 31.3
1363.752997	23 Feb 2024	-29.798	285 / 0.697	1627.0	280	1.84	16.16±0.20	77±16	1.1±0.3	1.64 / 3.20	219 / 30.6
1364.863166	24 Feb 2024	-30.087	285 / 0.913	1627.0	243	2.26	16.13±0.20	-21±19	0.9±0.3	1.43 / 3.05	169 / 18.6
1366.809540	26 Feb 2024	-30.114	286 / 0.293	1627.0	231	2.38	16.31±0.20	-119±21	-0.3±0.2	1.61 / 3.54	167 / 23.7
1367.794222	27 Feb 2024	-30.130	286 / 0.485	1627.0	263	2.03	16.31±0.20	14±21	-0.9±0.2	2.11 / 4.00	254 / 40.1
1368.768013	28 Feb 2024	-30.113	286 / 0.675	1627.0	262	2.01	16.09±0.20	124±18	0.6±0.3	1.73 / 3.02	226 / 38.4
1371.823004	02 Mar 2024	-30.279	287 / 0.270	1627.0	252	2.15	16.19±0.20	-185±16	-0.6±0.3	1.27 / 2.24	151 / 18.3
1890.097376	02 Aug 2025	25.411	388 / 0.338	1627.0	262	2.09	16.13±0.20	-140±18	-0.9±0.3	1.49 / 2.65	194 / 32.1
1891.134265	03 Aug 2025	25.614	388 / 0.540	1627.0	241	2.36	16.21±0.20	114±20	-0.3±0.3	1.47 / 2.06	144 / 18.0
1892.128748	04 Aug 2025	25.862	388 / 0.734	1627.0	200	2.93	15.26±0.20	163±24	0.4±0.3	1.44 / 1.67	139 / 18.9
1893.115636	05 Aug 2025	26.117	388 / 0.927	1627.0	295	1.88	16.05±0.20	-30±14	-0.3±0.3	1.26 / 2.11	178 / 29.7
1894.119577	06 Aug 2025	26.338	389 / 0.122	1627.0	268	2.06	16.58±0.20	-132±15	-0.3±0.3	1.19 / 1.97	107 / 11.8
1918.100650	30 Aug 2025	29.569	393 / 0.799	1627.0	297	1.80	15.85±0.20	56±19	0.1±0.3	2.19 / 4.74	350 / 66.3
1919.117444	31 Aug 2025	29.561	393 / 0.997	1627.0	230	2.54	16.37±0.20	-116±23	0.7±0.3	1.68 / 4.12	303 / 57.3
1921.060121	02 Sep 2025	29.708	394 / 0.376	1627.0	269	2.06	16.32±0.20	-94±17	-0.3±0.3	1.43 / 2.57	164 / 23.8
1922.102829	03 Sep 2025	29.625	394 / 0.579	1627.0	288	1.86	16.28±0.20	213±16	0.4±0.3	1.53 / 2.83	163 / 21.5
1923.129255	04 Sep 2025	29.558	394 / 0.779	1627.0	307	1.93	15.84±0.20	138±15	0.7±0.3	1.38 / 2.47	225 / 34.9
1924.093675	05 Sep 2025	29.626	394 / 0.968	1627.0	277	1.97	16.29±0.20	-3±14	0.2±0.3	1.11 / 1.96	160 / 26.3
1925.138891	06 Sep 2025	29.498	395 / 0.171	1627.0	275	2.25	16.76±0.20	-112±16	-0.7±0.3	1.18 / 2.08	142 / 21.8
1926.069436	07 Sep 2025	29.628	395 / 0.353	1627.0	268	2.05	16.37±0.20	-114±16	-0.5±0.3	1.29 / 1.89	103 / 11.6
1927.132970	08 Sep 2025	29.445	395 / 0.560	1627.0	280	1.98	16.18±0.20	188±16	-0.2±0.3	1.39 / 2.19	197 / 33.9
1928.016337	09 Sep 2025	29.647	395 / 0.733	1627.0	267	2.08	15.94±0.20	202±17	0.5±0.3	1.42 / 2.17	176 / 36.5
1929.050961	10 Sep 2025	29.535	395 / 0.934	1627.0	286	1.90	16.40±0.20	58±17	-0.3±0.3	1.64 / 3.09	223 / 50.6
1930.120355	11 Sep 2025	29.315	396 / 0.143	1627.0	286	1.90	16.95±0.20	-170±16	-0.5±0.3	1.56 / 2.51	205 / 36.2
1931.090549	12 Sep 2025	29.319	396 / 0.332	1627.0	230	2.32	16.48±0.20	-92±21	-0.4±0.3	1.74 / 2.74	190 / 30.5
1934.092710	15 Sep 2025	29.055	396 / 0.917	1627.0	268	2.08	15.81±0.20	8±16	0.2±0.3	1.34 / 1.93	238 / 45.6
1935.094710	16 Sep 2025	28.947	397 / 0.113	1627.0	266	2.10	16.81±0.20	-100±18	-0.7±0.3	1.51 / 2.06	215 / 41.6
1953.068354	04 Oct 2025	25.663	400 / 0.618	1627.0	247	2.32	15.71±0.20	269±17	0.7±0.4	1.23 / 2.48	99 / 8.2
1954.062369	05 Oct 2025	25.417	400 / 0.812	1627.0	266	2.04	15.72±0.20	99±14	0.2±0.3	1.05 / 1.84	111 / 16.3
1955.087395	06 Oct 2025	25.079	401 / 0.012	1627.0	264	2.10	16.10±0.20	-71±15	-0.2±0.3	1.06 / 1.55	157 / 26.3
1956.038567	07 Oct 2025	24.937	401 / 0.197	1627.0	279	1.95	15.91±0.20	-127±18	-0.3±0.3	1.74 / 2.78	194 / 27.7
1957.060051	08 Oct 2025	24.595	401 / 0.396	1627.0	253	2.20	15.86±0.20	9±22	-0.5±0.3	1.95 / 3.10	197 / 30.8
1958.135108	09 Oct 2025	24.103	401 / 0.606	1627.0	266	2.06	15.58±0.20	261±19	0.6±0.3	1.71 / 2.60	178 / 28.3
1959.081662	10 Oct 2025	23.950	401 / 0.790	1627.0	169	4.14	15.17±0.20	187±41	0.7±0.3	1.93 / 3.06	252 / 46.6
1961.068513	12 Oct 2025	23.372	402 / 0.178	1627.0	291	1.99	16.31±0.20	-155±18	-0.3±0.3	1.68 / 2.69	227 / 38.2
1963.134959	14 Oct 2025	22.545	402 / 0.581	1627.0	305	1.78	15.45±0.20	276±20	1.1±0.4	2.29 / 3.82	245 / 39.3
1980.040457	31 Oct 2025	16.193	405 / 0.878	1627.0	231	2.47	15.99±0.20	20±22	0.3±0.3	1.60 / 3.04	161 / 27.3
1980.988459	01 Nov 2025	15.905	406 / 0.062	1627.0	303	1.71	16.69±0.20	-67±15	-0.6±0.3	1.56 / 3.26	169 / 22.0
1981.936093	02 Nov 2025	15.605	406 / 0.247	1627.0	267	2.00	16.90±0.20	-137±19	-0.9±0.3	1.77 / 3.39	173 / 25.8
1983.067733	03 Nov 2025	14.785	406 / 0.468	1627.0	165	3.92	16.49±0.20	64±35	-0.5±0.3	1.65 / 2.31	110 / 10.8
1983.998058	04 Nov 2025	14.533	406 / 0.649	1627.0	235	2.50	15.88±0.20	258±23	1.3±0.3	1.67 / 2.85	129 / 16.5
1984.908775	05 Nov 2025	14.331	406 / 0.827	1627.0	172	3.47	15.64±0.20	124±34	0.4±0.4	1.94 / 3.73	190 / 35.6
1985.896779	06 Nov 2025	13.913	407 / 0.200	1627.0	154	3.91	16.27±0.20	-31±34	1.0±0.4	1.58 / 3.34	234 / 41.4
1987.104494	07 Nov 2025	12.850	407 / 0.255	1627.0	260	2.19	16.41±0.20	-193±19	1.1±0.3	1.53 / 2.46	205 / 32.3
1988.101042	08 Nov 2025	12.389	407 / 0.450	1627.0	246	2.24	16.61±0.20	26±18	-1.1±0.3	1.36 / 2.34	123 / 12.8
1989.047462	09 Nov 2025	12.059	407 / 0.634	1627.0	211	2.66	16.02±0.20	226±21	1.1±0.3	1.36 / 2.38	133 / 15.0
1990.153093	10 Nov 2025	11.327	407 / 0.850	1627.0	245	2.25	16.10±0.20	108±18	0.2±0.3	1.36 / 2.63	173 / 23.9
1991.018669	11 Nov 2025	11.176	408 / 0.018	1627.0	244	2.25	16.42±0.20	-1±15	0.4±0.3	1.04 / 1.88	92 / 7.2
1992.097601	12 Nov 2025	10.476	408 / 0.229	1627.0	233	2.29	16.90±0.20	-143±19	-1.2±0.3	1.42 / 2.37	189 / 26.3
1993.079506	13 Nov 2025	10.029	408 / 0.420	1627.0	200	2.66	16.28±0.20	7±22	-1.0±0.3	1.45 / 2.31	138 / 16.6

Notes. For each visit, we list the barycentric Julian date BJD, the UT date, the barycentric Earth RV (BERV), the rotation cycle c and phase ϕ (computed as indicated in Sec. 3), the total observing time t_{exp} , the peak S/N in the spectrum (in the H band) per 2.3 km s⁻¹

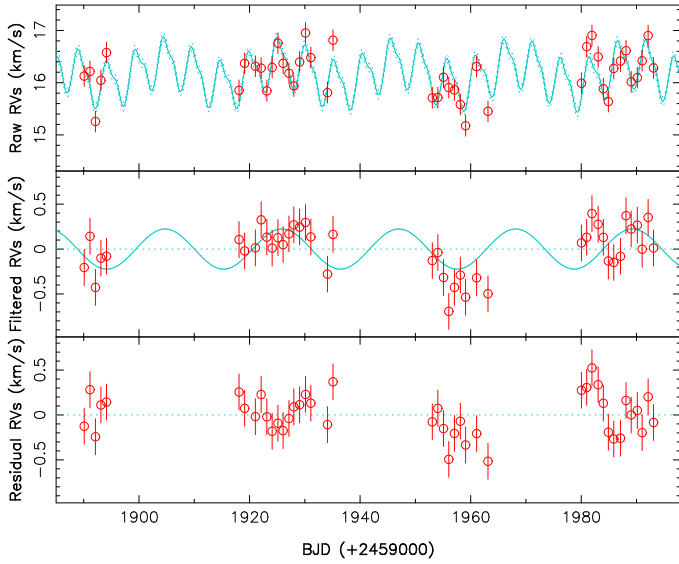


Fig. C.1: Same as Fig. 4, zooming-in on the 2025 data

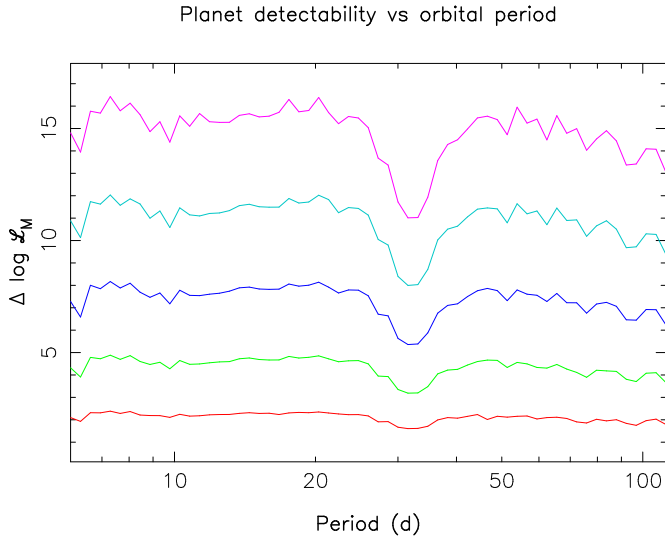


Fig. C.2: Logarithmic Bayes factor $\Delta \log \mathcal{L}_M$ as a function of orbital period for planet RV signatures of semi-amplitudes 0.10 (red), 0.15 (green), 0.20 (blue), 0.25 (cyan), and 0.30 km s^{-1} (purple), once averaged over all phases. Note the drop in $\Delta \log \mathcal{L}_M$ at orbital periods close to the synodic period of the Moon.

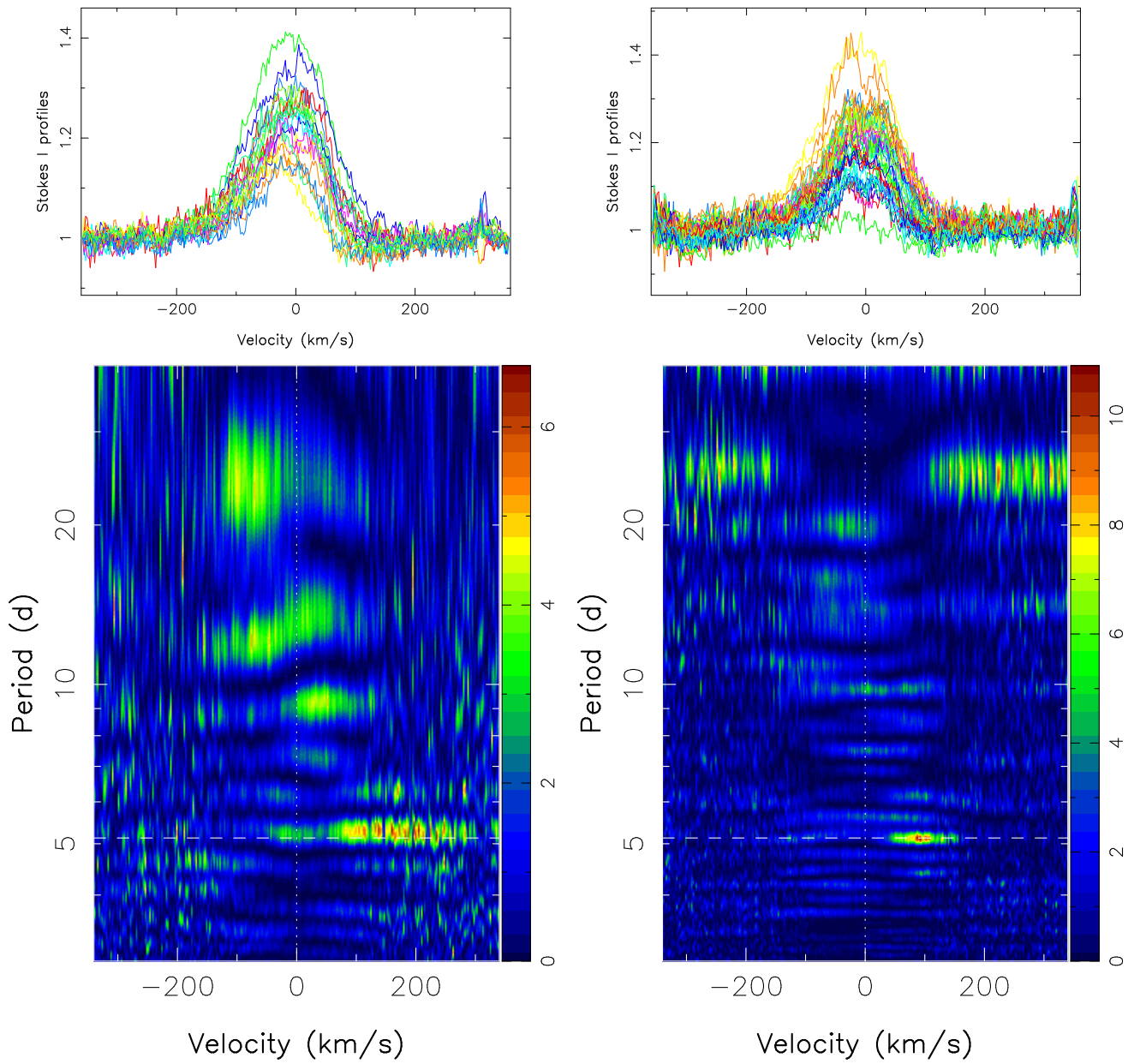


Fig. D.1: Same as Fig. 7 for the 2268 nm Bry line (left: 2024, right: 2025).

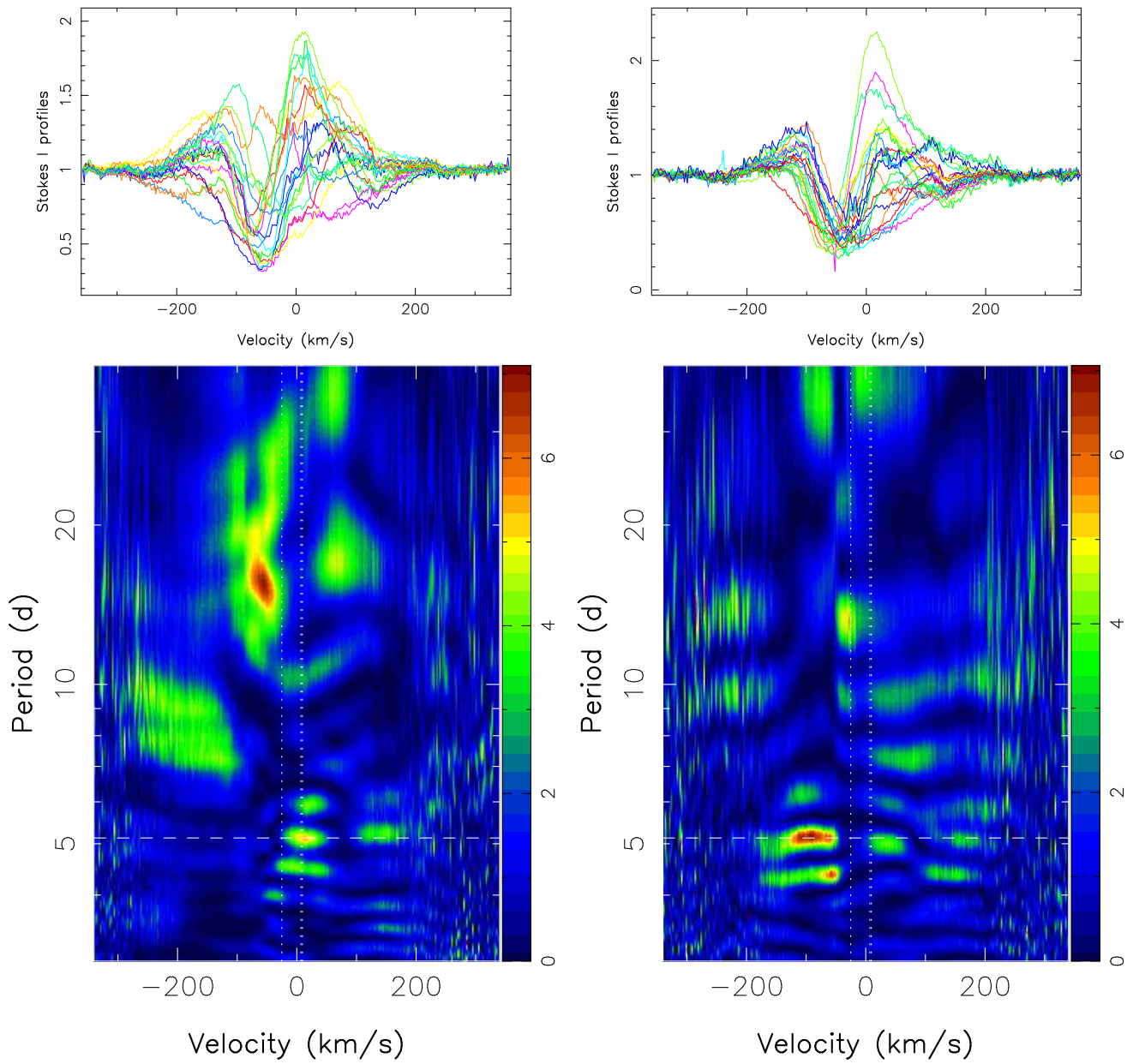


Fig. D.2: Same as Fig. 7 for the first (left panel) and second (right panel) half of the 2025 season data set.

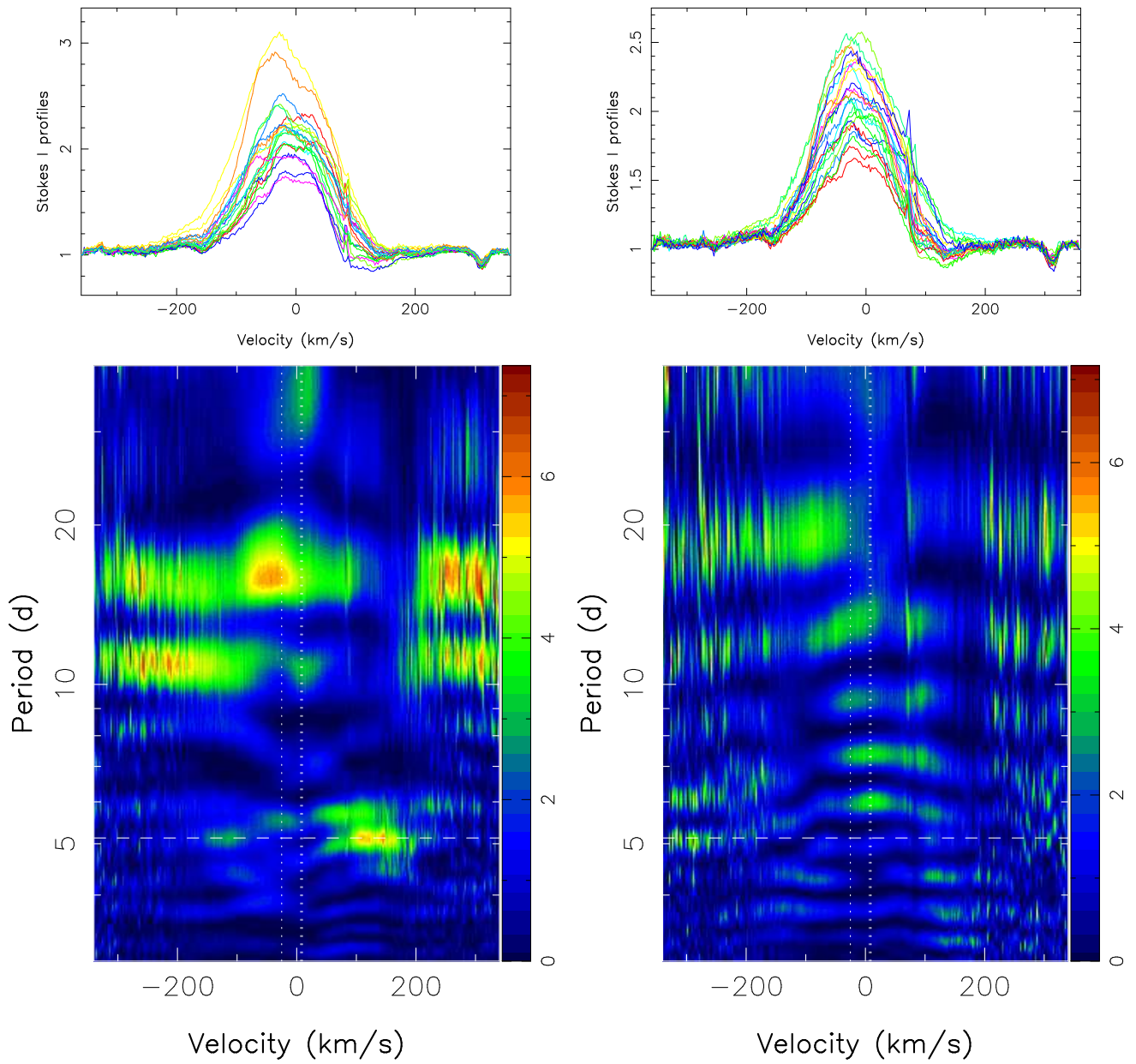


Fig. D.3: Same as Fig. D.2 for the 1282 nm Pa β line (left: first half of 2025, right: second half).

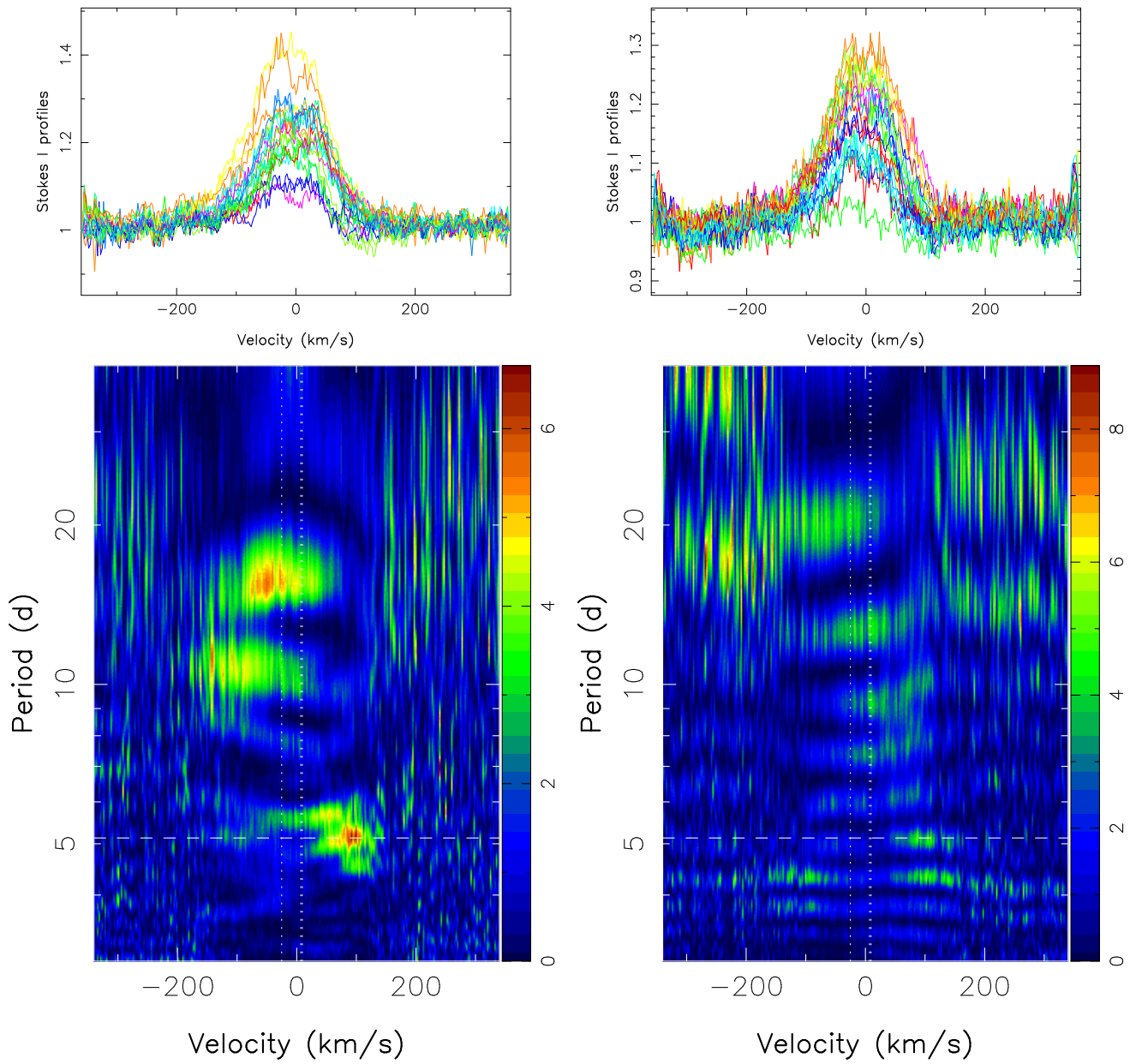


Fig. D.4: Same as Fig. D.2 for the 2268 nm Bry line (left: first half of 2025, right: second half).